https://doi.org/10.5194/egusphere-2026-3541
Preprint. Discussion started: 9 July 2026
© Author(s) 2026. CC BY 4.0 License.

Implementing Marine Aerosol Ice Nucleation Parametrizations in the Unified Model: Mitigating the Cloud Radiative Bias During a Case Study Over the Southern Ocean

Zhangcheng Pei[1], Sonya L. Fiddes[1], Marc D. Mallet[2], Matthew T. Woodhouse[3], Simon P. Alexander[4,1], Alain Protat[5,1], Kalli Furtado[6], and Paul R. Field[7]

[1]Australian Antarctic Program Partnership, Institute for Marine and Antarctic Studies, University of Tasmania, Hobart, Australia
[2]Bureau of Meteorology, Hobart, Australia
[3]Environment, CSIRO, Aspendale, Australia
[4]Australian Antarctic Division, Kingston, Australia
[5]Bureau of Meteorology, Melbourne, Australia
[6]National Oceanography Centre, Southampton, UK
[7]Met Office, Exeter, UK

Correspondence: Zhangcheng Pei (zhangcheng.pei@utas.edu.au)

Abstract.

Mixed-phase clouds over the Southern Ocean profoundly influence Earth's radiative balance, yet climate models persistently exhibit a positive surface shortwave radiation bias driven by over-glaciation in mixed-phase clouds. Addressing this bias requires accurate representation of ice-nucleating particles (INPs). This study presents the first online implementation of aerosol-aware marine INP parametrizations derived interactively from sea spray and marine organic aerosols within the high-resolution Unified Model. Using CAPRICORN-2 shipborne observations, we demonstrate that the default INP scheme overestimates INP concentrations by up to four orders of magnitude, causing a severely underestimated liquid water path. In contrast, empirical Antarctic and deterministic marine INP schemes reproduce the low INP concentrations typical of the pristine Southern Ocean, improving cloud and radiative properties. Crucially, microphysical and radiative responses to these INP reductions are strongly regime-dependent. In deep, pre-frontal mixed-phase clouds, suppressing INP concentrations effectively inhibits cloud glaciation, significantly enhancing supercooled liquid water and largely mitigating the surface shortwave radiation bias. However, in shallow, post-frontal stratocumulus clouds, altering INP parametrization yields negligible improvements. Radiosonde evaluations reveal this insensitivity is driven by several model deficits, including systematically smoothed boundary layer inversions leading to excessive dry air entrainment, exacerbated by underestimated cyclonic moisture transport. Consequently, these shallow clouds are thermodynamically starved of water vapor, rendering microphysical INP adjustments ineffective. Ultimately, fully resolving Southern Ocean cloud-radiation biases requires synergistic advancements in representing aerosols, boundary layer physics and large-scale meteorological forcings.

1 Introduction

The Southern Ocean (SO) plays a major role in the Earth's radiative balance. This region is characterized by ubiquitous low-level mixed-phase clouds, which contain a complex mixture of ice and supercooled liquid water (SLW) (Vergara-Temprado et al., 2018; Mace et al., 2021). A long-standing issue is that climate models consistently overestimate the downward shortwave (SW) radiation at the SO surface when compared to satellite observations (Bodas-Salcedo et al., 2014; Trenberth and Fasullo, 2010; Fiddes et al., 2022; Pei et al., 2023). This persistent bias is primarily linked to the misrepresentation of low- and mid-level mixed-phase clouds, which govern the overall cloud radiative effect over the SO (Bodas-Salcedo et al., 2016; Kay et al., 2016). These radiative errors directly hinder accurate forecasts of regional sea surface temperatures (SSTs) (Hyder et al., 2018). Furthermore, much of the uncertainty regarding Equilibrium Climate Sensitivity (ECS) in the recent Coupled Model Intercomparison Project Phase 6 (CMIP6) is driven by discrepancies in the SW radiative feedback of these SO low-level clouds (Zelinka et al., 2020; Gettelman et al., 2019).

In recent years, numerous studies have investigated how to better simulate mixed-phase clouds over the SO in climate models. These efforts generally fall into three categories. First, refining the representation of aerosols which act as cloud condensation nuclei (CCN). Accurate simulated concentrations of CCN are crucial because they help determine cloud droplet number concentrations, directly modulating cloud reflectivity and governing indirect aerosol-cloud interactions (McCoy et al., 2015; Fiddes et al., 2025). Second, improving cloud microphysical parameterizations. Processes such as the Wegener-Bergeron-Findeisen (WBF) mechanism, riming, vapor deposition, and secondary ice production (SIP) interactively control the liquid-ice phase partitioning and precipitation rates. For instance, enhanced SIP can increase ice crystal concentrations by orders of magnitude, which then rapidly depletes SLW through the WBF process (Sotiropoulou et al., 2021; Zhao et al., 2023). Furthermore, altering how well mixed the clouds are essentially impacts the cloud radiative effect (Smith et al., 2025). Third, addressing dynamical processes. Boundary layer parameterizations, cloud-top turbulence, and subgrid relative humidity distributions directly regulate the generation and maintenance of SLW (Furtado et al., 2016; Furtado and Field, 2017). Enhanced turbulence, for instance, is critical for maintaining liquid water in stratiform clouds and counteracting the rapid depletion of liquid droplets by ice growth (Atlas et al., 2020; Vignon et al., 2021). While these advancements have successfully improved the simulated liquid water content in SO mixed-phase clouds to some extent, the persistent cloud radiative bias remains incompletely solved.

The formation of ice crystals in mixed-phase clouds has a profound impact on cloud structure and radiative properties. Due to a lower saturation vapor pressure over ice compared to liquid water, ice crystals grow rapidly at the expense of supercooled liquid droplets known as the WBF process (Storelvmo and Tan, 2015). Larger ice particles subsequently precipitate and collect smaller liquid droplets through the riming process. These processes together efficiently deplete the liquid water content, ultimately reducing cloud albedo. The initial glaciation of these clouds requires ice-nucleating particles (INPs), which serve as seeds for heterogeneous ice formation. In mixed-phase clouds, immersion freezing, where an INP initiates freezing from within a supercooled liquid droplet, is recognized as the dominant nucleation mechanism (Murray et al., 2012; Kanji et al., 2017). Globally, INPs originate from diverse terrestrial sources, including mineral dust, bacteria, biomass burning, and agricultural soils (Hoose and Möhler, 2012). Nevertheless, over the remote SO, where continental aerosol are extremely scarce, marine

https://doi.org/10.5194/egusphere-2026-3541
Preprint. Discussion started: 9 July 2026
© Author(s) 2026. CC BY 4.0 License.

aerosols become the primary driver of ice formation. Sea spray aerosol (SSA), which comprises both biogenic organic material and sea salt emitted from the ocean surface via bubble bursting, is a critical source of INPs in this pristine marine environment (Burrows et al., 2013; DeMott et al., 2016).

Given the crucial role of these marine aerosols, the characteristics of INPs in pristine environments have received significant attention in recent years. Through field sampling and laboratory analysis, Wilson et al. (2015) revealed that organic matter released by marine phytoplankton, which is highly enriched in the sea surface microlayer (SML), possesses strong ice-nucleating abilities. Their findings demonstrated that bubble bursting efficiently transfers these biogenic materials into the atmosphere, serving as an active marine source of INPs. McCluskey et al. (2018b) found that the ice-nucleating ability of SSA is intrinsically linked to ocean biological activity. They identified distinct marine INP species associated with SSA, including an organic molecule that coats sea salt, and a heat-labile, marine microbial INP that remains active at temperatures warmer than -20 °C. Observations within the SO marine boundary layer confirmed that these pristine INP populations are extremely sparse and are almost entirely dominated by marine sources (McCluskey et al., 2018a). To quantitatively represent these emissions, McCluskey et al. (2018b) developed an INP parameterization based on temperature and SSA surface area concentrations. Using clean-sector measurements from the Mace Head Research Station in the North Atlantic, their formulation revealed that the ice nucleation site density of marine aerosols is approximately three orders of magnitude lower than that of mineral dust. More recently, Vignon et al. (2021) developed an empirical INP parameterization (V21) based on in-situ observations off Mawson Station in East Antarctica. Although this scheme is only temperature-dependent, it yields INP concentrations that are three to five orders of magnitude lower than classic parameterizations derived from Northern Hemisphere terrestrial environments.

A wide range of climate models, whether global or high-resolution regional models, employ empirically temperature-dependent ice nucleation parameterizations, such as those proposed by Cooper (1986) or Meyers et al. (1992). These schemes do not account for variations in aerosol species or concentrations. Subsequently, they do not reflect the very low INP concentrations of pristine regions like the SO. Applying these empirical schemes in such environments leads to an overestimation of cloud ice.

Recent studies have incorporated more realistic, aerosol-aware INP parameterizations to evaluate their impacts on cloud and radiative properties. These efforts generally fall into two approaches: offline evaluation and online implementation. In offline approaches, INP parameterizations are applied to pre-calculated aerosol mass or number outputs, focusing primarily on evaluating the predicted INP concentrations against observations. For instance, using the Global Model of Aerosol Processes (GLOMAP), Vergara-Temprado et al. (2017) demonstrated that marine organic aerosols dominate the INP population in pristine regions like the SO, despite being a relatively weak INP source globally. Similarly, McCluskey et al. (2023) evaluated marine and dust aerosol contributions in the Community Earth System Model (CESM) against ship and aircraft measurements over the SO, confirming that dust-only INP schemes are insufficient for representing pristine SO conditions. Herbert et al. (2025) recently used the UK Earth System Model (UKESM) to simulate the global, year-round distribution of immersion-freezing INPs from dust, marine, and black carbon sources. They found that the model matches field measurements much better when dust is treated as a realistic soil mixture of both mineral and organic components.

https://doi.org/10.5194/egusphere-2026-3541
Preprint. Discussion started: 9 July 2026
© Author(s) 2026. CC BY 4.0 License.

The online implementation directly couples INP schemes with cloud microphysics, allowing INPs to dynamically interact with cloud, precipitation, and radiation processes. Using high-resolution regional models, Vignon et al. (2021), Hines et al. (2021), Pei et al. (2025a) and Smith et al. (2025) demonstrated that applying the Vignon et al. (2021) INP parameterization tailored to the Antarctic environment significantly improves the simulated liquid water path and radiative fluxes. Furthermore, Vergara-Temprado et al. (2018) exhibited substantial improvements in simulating SO frontal cloud systems by utilizing INP profiles from GLOMAP-mode that account for both dust and marine organic aerosols. While dust-aware ice nucleation has been increasingly implemented in models for both the SO and the Arctic (Gettelman et al., 2020; Hawker et al., 2021), dynamic marine-sourced INPs continues to be explored. Zhao et al. (2021) introduced marine organic aerosols (MOA) into CESM2 to investigate their role as CCN and INPs. Their results showed that MOA dominates immersion-mode ice nucleation in the high-latitude lower troposphere, playing a vital role in modulating the phase partitioning of mixed-phase clouds.

In this study, we present the first online implementation of sea spray and marine organic aerosols as INP sources within a coupled aerosol-cloud microphysics scheme in a high-resolution regional model. Simulations are conducted for a biologically active summer period over the high-latitude SO, characterized by strong cyclonic systems and diverse cloud regimes. This period is during Phase 2 of the Clouds Aerosols Precipitation Radiation and atmospheric Composition over the Southern Ocean (CAPRICORN-2) campaign, detailed fully by McFarquhar et al. (2021) and Mallet et al. (2025). Recently, Price et al. (2025) investigated similar CAPRICORN-2 case studies using a comparable high-resolution UM model with interactive aerosols. They demonstrated substantial underestimations in surface aerosol concentrations and cloud liquid water, attributing the cloud liquid biases primarily to meteorological deficiencies rather than aerosol or cloud microphysical properties. However, their experiments did not include the INP treatments introduced here. To build upon their findings, our model evaluation focuses primarily on the response of cloud phase, liquid and ice water paths, and radiative fluxes to the different INP parameterizations. The structure of this paper is as follows: Section 2 describes the observational datasets and model configurations. Section 3 presents the results and discussions, and Section 4 provides the conclusions and implications for future research.

2 Data and Methods

2.1 CAPRICORN-2 campaign

The CAPRICORN-2 campaign was conducted aboard the Research Vessel (RV) Investigator between 11 January and 21 February 2018. The voyage track extended from Hobart, Australia, southward to the sea-ice edge of East Antarctica. A comprehensive overview of the campaign and the instruments deployed was provided by McFarquhar et al. (2021). Our study utilizes a subset of these observations including the ship-based measurements of cloud, radiative fluxes, meteorological conditions, and aerosol properties. The specific instruments and data products are detailed below.

© Author(s) 2026. CC BY 4.0 License.

2.1.1 Cloud, Radiation, and Meteorology Observations

Cloud phase was determined by merging observations from the shipborne 95 GHz BASTA radar (Delanoë et al., 2016) and Leosphere R-MAN510 Raman UV polarization lidar (Alexander and Protat, 2018). Detailed technical specifications and calibration procedures for these instruments are documented by Noh et al. (2019) and Alexander et al. (2021). Radar often misses small liquid droplets, while lidar signals attenuate rapidly in optically-thick layers. Merging these two datasets overcomes their individual limitations, providing a more complete phase classification. After regridding the instrument data to uniform 15 m vertical resolution and 1 min temporal resolution and interpolating them with collocated ERA5 temperature profiles along the ship track, a phase-classification algorithm was applied to classify hydrometeor layers into warm liquid, SLW, ice, mixed-phase, ice/mixed-phase, and ice virga based on thresholds of radar reflectivity and lidar backscatter and depolarisation ratio (Alexander et al., 2021).

Liquid water path (LWP) is retrieved from the shipborne microwave radiometer (MWR) using the algorithm described by Mace et al. (2021). Ice water path (IWP) is estimated from BASTA radar reflectivity, along with using ERA5 temperatures, following Protat et al. (2007) and Pei et al. (2025b). Shipborne pyranometer and pyrgeometer provide continuous measurements of downwelling shortwave and longwave surface radiative fluxes, respectively.

Surface meteorological conditions, including air temperature, relative humidity, pressure, and wind speed, are provided by the underway meteorological suite mounted on the RV Investigator (Protat et al., 2020). Six-hourly launched radiosondes complement surface measurements by profiling the vertical thermodynamic structures of the troposphere throughout the campaign.

2.1.2 INP Observations

INPs were collected on aerosol filters and subsequently measured utilizing an Ice Spectrometer between -30 °C and -10 °C. Real-time INP concentrations at -30 °C were measured with a Continuous Flow Diffusion Chamber. Further details are available in Moore et al. (2024).

2.2 Unified Model Regional Nesting Suite

The United Kingdom Met Office's Unified Model Regional Nesting Suite (UM RNS) is a numerical atmosphere and land model, designed for high resolution forecasting and research applications across different grid resolutions and geographical domains (Bush et al., 2020, 2023, 2025). The UM is non-hydrostatic and fully compressible with a semi-Lagrangian dynamical formulation for the deep atmosphere. The discretized equations of motion are solved through the Even Newer Dynamics General Atmospheric Modelling of the Environment (ENDGame) (Wood et al., 2014). Land surface processes are represented by the Joint UK Land Environment Scheme (JULES) (Best et al., 2011; Clark et al., 2011).

We utilize the Regional Atmosphere and Land configuration 3.2 (RAL3.2) and UM version 13.0, comprehensively documented in Bush et al. (2025). This configuration features a bimodal cloud fraction scheme which identifies moist and dry Gaussian modes to diagnose sub-grid cloud water content and cloud fraction (Van Weverberg et al., 2021). It also couples directly with the double moment Cloud AeroSol Interacting Microphysics (CASIM) scheme, which is detailed later in Section

2.2.2. Key updates in the RAL3.2 include the implementation of a blended boundary layer scheme (Boutle et al., 2014) and an adaption of the radiative transfer scheme (Edwards and Slingo, 1996) to operate interactively with CASIM (Bush et al., 2025).

The GLOMAP-mode microphysical aerosol scheme (Mann et al., 2010, 2012) was utilized to prognose the mass and number concentrations of aerosol species. The GLOMAP-mode scheme is coupled with CASIM via a one-way interaction. Specifically, GLOMAP-mode supplies the aerosol fields and cloud droplet number concentrations (CDNC) to CASIM. While CASIM utilizes these prescribed aerosol fields for cloud microphysical processes, it does not directly modify the aerosol populations (Gordon et al., 2020). Section 2.2.3 provides a full description of the aerosol scheme.

2.2.1 Model Setup

The model was run from 28 January to 2 February 2018 to simulate a CAPRICORN-2 case study characterized by pronounced biological and cyclonic activity. The simulations consist of 48-hour forecasts initialized at 0000 UTC daily. The first 24 hours of each forecast are discarded as spin-up. The UM RNS operates with a 75-second time step and we output all the data at 10-minute intervals. The domain utilizes a rotated polar grid with 400 x 800 grid points in latitude x longitude centred at 141°E, -64.5°S. The horizontal resolution is approximately equivalent to 1.5 km. Deep convective mixing is explicitly resolved at this grid spacing, allowing the subgrid convection parameterization to be deactivated. The vertical grid comprises 90 stretched levels reaching an altitude of 40 km, with the lowest model level positioned at 5 m and 16 levels in the first 1000 m.

Initial and lateral boundary conditions are provided by the global configuration of the UM. This driving model operates at an N216 resolution (approximately 60 km at the equator) using the Global Atmosphere (GA) 8.0 science configuration (Willett et al., 2026), and is nudged towards ERA5 reanalysis. Figure 1 exhibits the model domain (red box) and the CAPRICORN-2 ship track (black line). These are overlaid on the mean January-February 2018 chlorophyll concentrations from the Moderate Resolution Imaging Spectroradiometer (MODIS) product (green shading) (NASA Ocean Biology Processing Group, 2025) and the sea ice concentration exceeding 15% from the National Snow and Ice Data Center (NSIDC) dataset on 1 February 2018 (blue shading) (Meier et al., 2026).

To better represent the conditions over the high latitude SO, we modified the default initial fields for SSTs, sea ice concentration (SIC), and dimethyl sulfide (DMS). We replaced the default HADISST monthly climatology with the Reynolds high-resolution Optimally Interpolated SST (OISST) dataset (Huang et al., 2021). This modification more accurately captures the accelerated decline in Antarctic sea ice observed after 2016 (Doddridge et al., 2025). Similarly, the underlying DMS climatology was updated from the Lana et al. (2011) to the Hulswar et al. (2022), which provides higher and more realistic DMS emission concentrations along the Antarctic coast. Preliminary testing confirmed that updating these boundary conditions substantially improves the simulated thermodynamic profiles, cloud properties, radiative fluxes, and ambient aerosol concentrations. Nevertheless, evaluation of these updates falls outside the primary scope and thus is not detailed in this manuscript.

2.2.2 Cloud Microphysics

The double-moment CASIM scheme simulates both mass and number concentrations across five hydrometeor categories: cloud liquid, rain, ice, snow, and graupel. CASIM also represents cloud microphysical processes such as condensation, deposition,

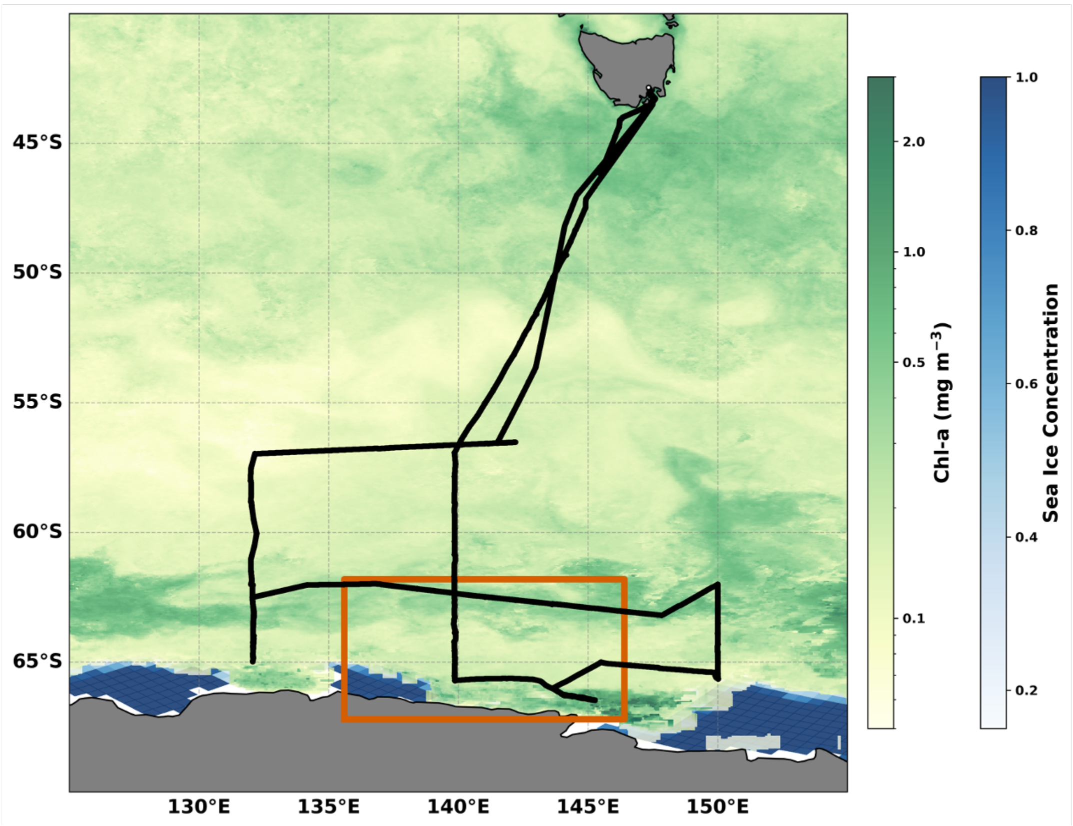

Figure 1. Overview of the CAPRICORN-2 voyage track and the UM model domain. The thick black line illustrates the ship track of the RV Investigator. The solid red box shows the model domain. Background green shading represents the mean MODIS Aqua chlorophyll-a concentrations (logarithmic scale, $\mathrm{mg\,m^{-3}}$) averaged over January and February 2018. Blue shading denotes the daily sea ice concentration on 1 February 2018 derived from the NSIDC dataset, masked for concentrations exceeding 15%. Continent is masked in dark grey.

sublimation, autoconversion, riming, and sedimentation (Field et al., 2023). For cloud activation, the model can apply either a fixed or dynamically activated cloud droplet number from online prognostic aerosol fields utilizing the Gordon et al. (2020) approach.

For ice nucleation processes, primary heterogeneous ice nucleation initiates at temperatures below -8°C, following the Cooper (1986) INP parameterization. CASIM accounts for the immersion freezing of rain droplets into graupel, while homogeneous freezing is activated below –38° C. Secondary ice production in CASIM is only represented by the Hallett-Mossop rime-splintering effect between –2.5°C and –7.5°C (Hallett and Mossop, 1974).

2.2.3 Aerosol Microphysics

The GLOMAP-mode aerosol scheme employs a two moment, pseudomodal framework (Mann et al., 2010, 2012). It prognoses the mass and number concentrations of sulfate, sea salt, black carbon and organic matter across five internally mixed modes:

https://doi.org/10.5194/egusphere-2026-3541
Preprint. Discussion started: 9 July 2026
© Author(s) 2026. CC BY 4.0 License.

soluble nucleation, Aitken, accumulation, coarse, and insoluble Aitken. GLOMAP-mode explicitly resolves the aerosol size distribution and simulates key processes including primary emission, secondary formation, condensation, coagulation, cloud processing, and removal via dry and wet deposition (Mann et al., 2010).

Oceanic DMS emission fluxes rely on the parameterization by Liss and Merlivat (1986). As detailed previously in Section 2.2.1, we update the surface water DMS climatology to the Hulswar et al. (2022), replacing the older Lana et al. (2011) dataset (Fiddes et al., 2025; Bhatti et al., 2023). The primary marine organic (PMO) aerosol emission is turned on and taking into account organic matter (Mulcahy et al., 2020). Sea spray aerosol (SSA) emission fluxes are calculated using the wind speed parameterization source function developed by Gong (2003), incorporating the updated sea salt density from Mulcahy et al. (2020). Free tropospheric new particle formation (NPF) occurs via the binary homogeneous nucleation of water and sulfuric acid according to Kulmala et al. (1998), while boundary layer NPF is not turned on. A binning method developed by Woodward (2001) calculates dust emissions externally to the GLOMAP-mode scheme. Other trace gases and primary aerosol emissions from anthropogenic and terrestrial sources including volcanic and industrial $\mathrm{SO_2}$, biomass burning, and monoterpenes are prescribed according to CMIP6 protocols (Eyring et al., 2016).

2.2.4 Heterogeneous Ice Nucleation Parameterizations

To investigate the sensitivity of SO mixed-phase clouds to primary ice formation, four distinct heterogeneous ice nucleation parameterizations are evaluated within the UM CASIM microphysics framework. These schemes range from empirical temperature-dependent to dynamical aerosol-aware parameterizations. All INP concentrations discussed in this study refer to the immersion freezing INP.

Cooper (1986)

The default UM RAL3.2 configuration employs the Cooper (1986) (hereafter C86) empirical parameterization. C86 is derived from in situ aircraft observations of ice crystal concentrations collected over the continental regions in the Northern Hemisphere, inherently assuming a background aerosol population dominated by highly efficient terrestrial aerosols such as mineral dust. It implicitly adopting a direct one-to-one relationship where each activated INP produces a single ice crystal. C86 parameterization serves as a bulk proxy for primary ice production. Recent field observations by Daily et al. (2026) validate that the primary ice crystal concentrations can serve as a proxy for INP populations under specific conditions such as during the initial development phases of convective clouds over Magdalena Mountain, New Mexico, USA. C86 determines the number concentration of active INPs ($N_{\mathrm{INP,C86}}$, in $\mathrm{L^{-1}}$) solely as an exponential function of the ambient temperature (T, in $^{\circ}\mathrm{C}$):

$$N_{\mathrm{INP,C86}} = 0.005\exp(-0.304 \times T) \tag{1}$$

This parameterization is bounded between $-8\,^{\circ}\mathrm{C}$ and $-38\,^{\circ}\mathrm{C}$. While this approach effectively captures the general temperature dependence of heterogeneous ice nucleation, it fundamentally neglects the role of aerosol composition, size, and supersaturation states. Originally derived from airborne measurements. Consequently, applying C86 to the pristine marine boundary layer of the SO often results in substantial overestimations of primary ice production (McCluskey et al., 2018a).

Vignon et al. (2021)

To address the systematic overestimations of ice crystals produced by continental-based INP schemes in the model, Vignon et al. (2021) (hereafter V21) developed a observation-based empirical parameterization tailored specifically for the high-latitude Southern Ocean environment. This scheme derives from a direct temperature fit of INP concentrations measured near Mawson Station, Antarctica (67.6S,62.9E), during the Measurements of Aerosols, Radiation and Clouds over the Southern Ocean (MARCUS) campaign. The active INP number concentration ($N_{\mathrm{INP,V21}}$, in $\mathrm{sL^{-1}}$) is prescribed as a piecewise function of the ambient temperature (T, in $^\circ\mathrm{C}$):

$$\log_{10}(N_{\mathrm{INP,V21}}) = \begin{cases} -0.14(T - T_1) - 2.88, & \text{if } T > T_1 \\ -0.31(T - T_1) - 2.88, & \text{if } T_2 \leq T \leq T_1 \\ 0.0, & \text{if } T < T_2 \end{cases} \tag{2}$$

with $T_1 = -21.06\,^\circ\mathrm{C}$ and $T_2 = -30.35\,^\circ\mathrm{C}$. To prevent unrealistic extrapolations at extremely low temperatures, the scheme constrains the maximum INP concentration not to exceed $1\,\mathrm{sL^{-1}}$. This threshold aligns with the DeMott et al. (2010) predictions for low-aerosol concentrations and is physically grounded with SO observations from the first CAPRICORN campaign (McCluskey et al., 2018b).

Recent studies demonstrate that adopting the V21 scheme notably improves the simulation of cloud liquid water path and radiative fluxes in regional climate models over the high-latitude SO (Vignon et al., 2021; Smith et al., 2025; Pei et al., 2025a). Nevertheless, it inherently misses the variations of SSA INPs which can occur over the SO driven by synoptic conditions (Mallet et al., 2025).

Wilson et al. (2015)

The Wilson et al. (2015) parametrization (hereafter W15) links INP activity directly to biogenic organic material ejected from the SML. W15 relies on the assumption that marine biogenic organic matter, particularly submicron components, serves as an efficient source of atmospheric INPs under supercooled conditions. The parametrization establishes a temperature-dependent relationship between total organic carbon (TOC) mass and INP concentration. The active INP number concentration ($N_{\mathrm{INP,W15}}$, in $\mathrm{m^{-3}}$) is calculated as the product of a TOC active site density based on temperature (T, in $^\circ\mathrm{C}$) and the simulated ambient mass concentration of marine organic aerosols (M_{org}, in $\mathrm{g\,m^{-3}}$):

$$N_{\mathrm{INP,W15}} = M_{\mathrm{org}} \times \exp(11.2186 - 0.4459 \times T) \tag{3}$$

To implement the W15 parametrization in CASIM, we diagnose ambient immersion-freezing INP concentrations from the GLOMAP-mode aerosol fields. PMOA emissions are represented in GLOMAP-mode using the empirical parametrization developed by Gantt et al. (2012), which estimates the organic mass fraction of SSA as a function of the 10 m wind speed, ocean chlorophyll-a concentration, and the dry diameter of sea spray particles. The organic mass flux is subsequently calculated by multiplying the organic mass fraction by the volume flux and density of the SSA. Upon emission, the PMOA flux is allocated to the Aitken mode, with 25% to the soluble mode and 75% to the insoluble mode (Mulcahy et al., 2020). Because GLOMAP-mode tracks the total organic matter rather than outputting a PMOA tracer, the TOC required for W15 is estimated by summing the organic matter mass from the soluble Aitken and soluble accumulation modes. This approach effectively represents pristine marine emissions by selecting soluble, submicron particles. The combined organic mass is then converted to TOC using a standard OM/OC ratio of 1.4 (Gantt et al., 2012) and which can then be provided to CASIM to calculate INP concentration using W15 parametrization as above.

McCluskey et al. (2018b)

McCluskey et al. (2018b) (hereafter M18) introduces a parameterization based on SSA surface area tailored for pristine SO, representing immersion-mode INPs associated with organic molecules that coat SSA particles. M18 scheme predicts the INP number concentrations ($N_{\mathrm{INP,M18}}$, in m^{-3}) by multiplying a temperature-dependent ice nucleation surface site density (n_s, in m^{-2}) by the SSA total surface area concentration (S_{SSA}, in $\mathrm{m}^2\,\mathrm{m}^{-3}$):

$$N_{\mathrm{INP,M18}} = S_{\mathrm{SSA}} \times \exp(-0.545 \times T + 1.0125) \tag{4}$$

M18 requires the total surface area of the SSA particles, encompassing both the sea salt core and its organic coating. Nevertheless, as GLOMAP-mode does not explicitly resolve organic coatings on individual particles, we implement the McCluskey et al. (2023) method by assuming that organic coatings contribute minimally to the total SSA surface area. Moreover, Mallet et al. (2025) has shown a statistically robust relationship between INP concentration at -30 °C and submicron sea salt mass. Consequently, the simulated sea salt surface area serves as a physically robust proxy for S_{SSA}.

GLOMAP-mode provides the mass for specific aerosol species but only outputs the total number of aerosols for each mode. Both the mass and number are required to calculate the aerosol surface area. Following the method from McCluskey et al. (2023), we first compute the total aerosol surface area for the soluble accumulation and coarse modes. We then calculate the mass fraction of sea salt in each mode. By multiplying the total surface area by this mass fraction, we estimate the sea salt surface area for each mode. Adding these two modes together gives the total S_{SSA}. It should be noted that McCluskey et al. (2023) included sea salt in Aitken mode. Only the accumulation and coarse modes are used in this study as GLOMAP-mode does not provide sea salt emissions into the Aitken mode.

2.3 Reanalysis and Satellite Products

The mean sea level pressure and total cloud cover from the ERA5 reanalysis are used to investigate the synoptic conditions during the case study. Although ERA5 has known biases with representing the SO cloud occurrence (McDonald et al., 2025), its cloud cover field is used here solely to outline the broad synoptic frontal systems. Additionally, Moderate Resolution Imaging Spectroradiometer (MODIS) Aqua chlorophyll-a concentrations are mapped across the domain to indicate background biological productivity (Figure 1), which is a key driver for PMOA emissions. The daily sea ice concentrations from the National Snow and Ice Data Center (NSIDC) is derived to represent the sea ice extent during the austral summer (Figure 1).

© Author(s) 2026. CC BY 4.0 License.

2.4 EMC^2 simulated cloud phase

The Earth Model Column Collaboratory (EMC^2) is an open-source ground-based lidar and radar instrument simulator with subcolumn generator that can be used with both global climate models and high-resolution regional models (Silber et al., 2022). It was developed to support rigorous comparisons between models and observations while ensuring consistency with the physical assumptions embedded in the model.

In this study, implementation of EMC^2 utilizes high temporal resolution output of the microphysical variables required for radar and lidar forward calculations such as hydrometeor mass and number mixing ratios. The outputs were sampled every 10 minutes from the grid cell along the shiptrack during our case study in CAPRICORN-2. The simulator provides two methods for remote sensing calculations, involving a radiation scheme logic that generalizes hydrometeor fractions and uses bulk scattering calculations based on prescribed particle size distributions, whereas the other adopts a microphysics approach that performs single particle scattering calculations using the particle size distributions simulated by the model. Here, we employ the radiation scheme logic, which is applicable to both stratiform and convective cloud schemes, with key hydrometeor parameters including terminal fall velocity and shape parameter specifically tuned for CASIM (Field et al., 2023). Given the high spatial resolution of the UM model, one subcolumn is generated in EMC^2. A maximum-random overlap assumption is subsequently applied to extend cloud layers vertically within the subcolumn while preserving the vertical coherence of cloud and precipitation properties. Further details of the subcolumn generation and forward simulation are provided by Silber et al. (2022).

Using the simulated radar reflectivity, lidar backscatter, and depolarization ratio from EMC^2, the same cloud phase classification algorithm applied to the observations was also applied to the model output (Pei et al., 2025a). Briefly, lidar backscatter profiles were first calibrated to remove high-altitude noise, after which cloud layers were identified from the vertical structure of the backscatter signal following gradient and signal-to-noise threshold. Cloud phase was then determined from the relationship between layer-integrated lidar backscatter and depolarization ratio, with ERA5 temperature profiles used to distinguish "warm liquid" from "SLW" clouds. Finally, lidar and radar signals were combined so that SLW layers coexisting with radar signals were classified as "mixed-phase" clouds, while layers with fully attenuated lidar signals but detectable radar signals were assigned to an “ice or mixed-phase” category to account for possible existing SLW. More detail of cloud phase classification algorithms can be found in Guyot et al. (2022) and Knight et al. (2024).

3 Results

3.1 Cloud Regime Classification and Synoptic Condition

Here, we characterize the cloud regimes and synoptic conditions along the RV Investigator track during the case study to set the context for model evaluation. Figure 2a displays the cloud phase derived from the merged lidar-radar observations, providing a vertical cross-section of the observed cloud systems. Based on distinct cloud morphology and cloud base-top heights, we partitioned the case study into two cloud regimes: (1) the SLW period (light blue shading in Figure 2a), characterized by shallow marine boundary layer stratocumulus clouds dominated by SLW, occurring from 16:00 UTC on 28 January to 00:00 UTC on 30 January, and later from 12:00 UTC on 31 January to 02:00 UTC on 01 February; and (2) the MIX period (light orange shading in Figure 2a), dominated by deep glaciated frontal mixed-phase clouds, occurring from 08:00 UTC on 30 January to 12:00 UTC on January 31, and later from 10:00 UTC on 01 February to 00:00 UTC on 03 February.

To investigate the large-scale meteorological factors driving these distinct regimes, we illustrate the total cloud cover and mean sea level pressure from the ERA5 reanalysis (Figure 2b-e). Four specific synoptic snapshots, marked by vertical dashed lines in Figure 2a, show the typical conditions for the SLW periods (Fig 2b, d) and the MIX periods (Fig 2c, e). Furthermore, shipborne surface observations were utilized to validate the local meteorological environment as well as evaluate the performance of different model configurations (appendix Figure A1).

During the SLW periods, the ship was situated to the west of the departing low-pressure centres (Fig 2b, d), placing it within the cold sector of the extratropical cyclones during a post-frontal stage. As a result of strong post-frontal subsidence, the cloud layers were suppressed, forming stable, low-altitude SLW-dominated cloud systems (Fig 2a). The shipborne surface observations clearly reflected this cold sector environment, showing steadily declining air temperatures and relative humidity, increased surface pressure, and weaker wind speeds (black lines in Fig A1a, c, e, g) as the frontal systems moved away.

The MIX periods encompass the deeply glaciated cloud systems driven by the approach of low-pressure cyclone systems (Fig 2c, e). During these phases, the ship was positioned east of the low-pressure centres, situating it within the pre-frontal warm sector. Ahead of and along the advancing frontal boundaries, strong north-westerly winds advected warmer, moist air southwards, forcing intense dynamic uplift. This rapid ascent caused the cloud tops to extend up to 6 km (Fig 2a), exposing the cloud layers to extreme cold and triggering widespread glaciation. Surface observations corroborated this frontal passage, evidencing a drop in surface pressure, an increase in relative humidity and wind speeds, while surface temperatures exhibited fluctuations typical of frontal mixing (Fig A1).

3.2 Marine INP Representation in different parametrizations

Next, we examine how well the different INP parametrizations represent the INP populations over the high-latitude SO. Figure 3 presents the simulated INP concentrations for immersion freezing as a function of temperature across the entire case study, compared against the INP measurements collected during CAPRICORN-2. To ensure a consistent comparison, the ambient INP concentrations output by the model are converted to match the laboratory units of per standard litre ($\mathrm{s\,L^{-1}}$).

The observations (black dots) exhibit the low INP characteristics of the pristine SO, with concentrations predominantly ranging from 10^{-4} to $10^{0}\,\mathrm{sL^{-1}}$ between $-15\,^{\circ}\mathrm{C}$ and $-28\,^{\circ}\mathrm{C}$ (Figure 3). The C86 parametrization (light blue dots) exhibits a substantial overestimation of INP in this environment, overpredicting the INP concentration by approximately 2 to 4 orders of magnitude (Figure 3). Derived from measurements over the East Antarctic coast, the V21 scheme (yellow line) is able to represent the overall magnitude and trend of INP concentrations between $-30\,^{\circ}\mathrm{C}$ to $-15\,^{\circ}\mathrm{C}$. However, V21 still produces INP concentrations up to an order of magnitude higher than the observations within the specific range of $-30\,^{\circ}\mathrm{C}$ to $-20\,^{\circ}\mathrm{C}$ (Figure 3). Importantly, the observational data reveal substantial variability in INP concentrations at any given temperature, an inherent natural variance that is noticeably larger than what the parameterizations are able to represent.

https://doi.org/10.5194/egusphere-2026-3541
Preprint. Discussion started: 9 July 2026
© Author(s) 2026. CC BY 4.0 License.

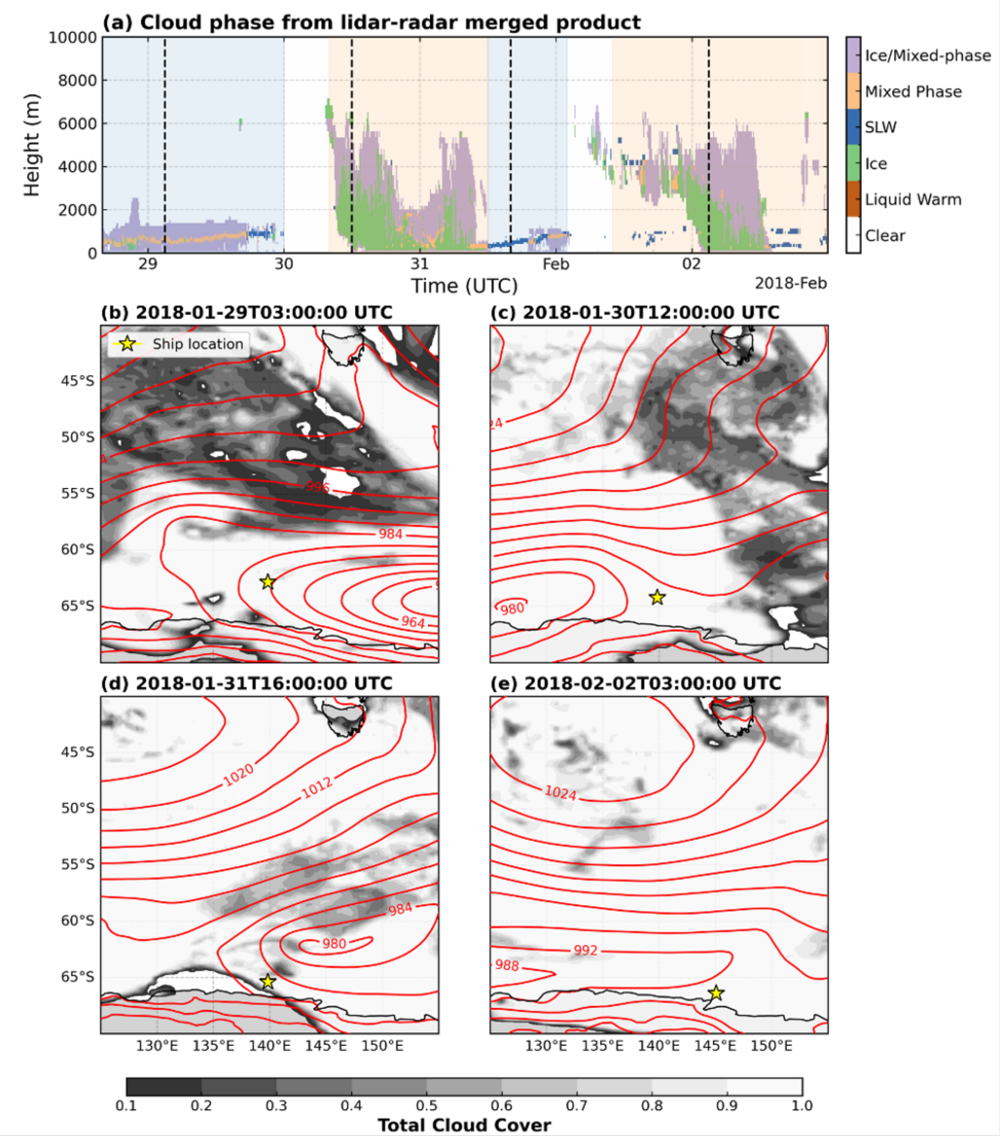

Figure 2. Overview of cloud structures and synoptic meteorological conditions during the case study. **(a)** Time-height cross-section of the cloud phase derived from the merged lidar-radar product. Colors indicate clear sky (white), liquid warm (brown), ice (green), supercooled liquid water (blue), mixed-phase (orange), and ice or mixed-phase (purple). Light blue and light orange background shading indicates the SLW and MIX periods, respectively. Vertical dashed lines denote the times of the synoptic snapshots shown in the lower panels. **(b)–(e)** Spatial distributions of total cloud cover (grayscale shading) and mean sea level pressure (MSLP; red contours in hPa) from the ERA5 reanalysis at four specific times. The yellow star indicates the location of the RV *Investigator*. Panels **(b)** and **(d)** illustrate the post-frontal environments during the shallow SLW periods, while panels **(c)** and **(e)** illustrate the pre-frontal environments during the deep MIX periods.

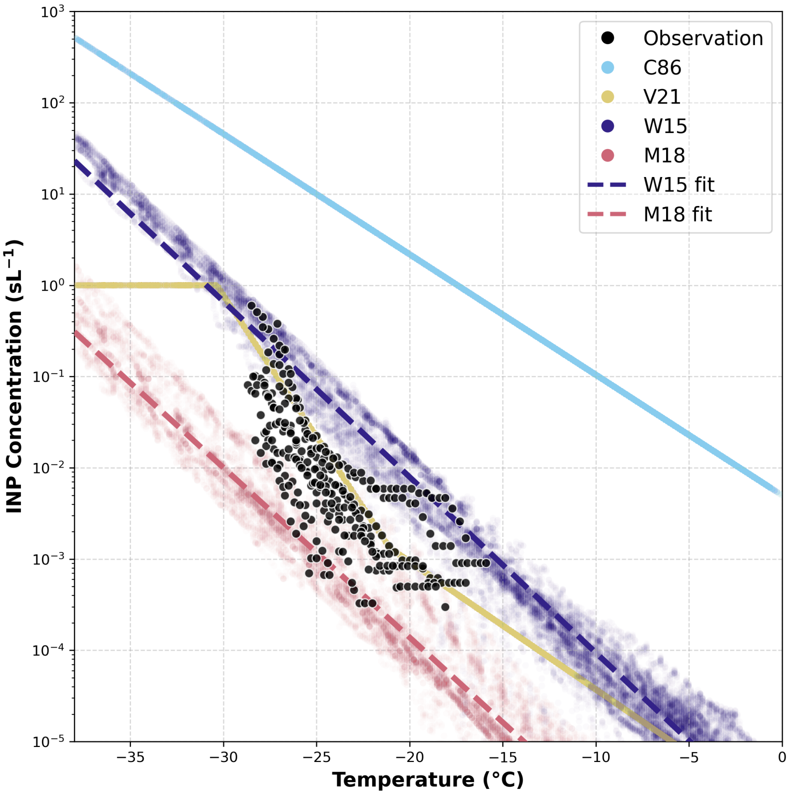

Figure 3. Evaluation of simulated immersion-freezing INP concentrations against shipborne filter-based measurements. The black dots represent the observed INP concentrations measured during the CAPRICORN-2 voyage. The light blue and yellow lines denote the INP concentrations predicted by the C86 and V21 parametrizations, respectively. The scattered red and dark blue points illustrate the INP concentrations from the M18 and W15 schemes, respectively. The corresponding dashed lines indicate the linear fits for the M18 and W15 outputs across the sampled temperature range. All simulated ambient INP concentrations have been converted to laboratory-equivalent units ($\mathrm{s\,L^{-1}}$) for consistent comparison.

The purple and red dots in Figure 3 exhibit the INP concentrations from the W15 and M18 schemes, respectively, with dashed lines illustrating the fitted relationship between temperature and INP concentrations. Unlike the static C86 and V21 schemes, these two aerosol-aware dynamical parametrizations show clear variability at any given temperature. This variability spans up to 1 order of magnitude for W15 and approximately 2 orders of magnitude for M18, although temperature still primarily drives the overall trend in both schemes (Figure 3).

This variability is directly linked to the underlying prognostic aerosol fields. Appendix Figure A2 shows the time-height profiles of the aerosol masses along the ship track used to calculate these schemes. For M18, we utilize the mass of sea salt in the soluble accumulation and coarse modes to represent SSA. For W15, we utilize the total organic matter in the soluble Aitken and accumulation modes, divided by 1.4 to represent TOC. The profiles reveal enhanced SSA emissions from the sea

https://doi.org/10.5194/egusphere-2026-3541
Preprint. Discussion started: 9 July 2026
© Author(s) 2026. CC BY 4.0 License.

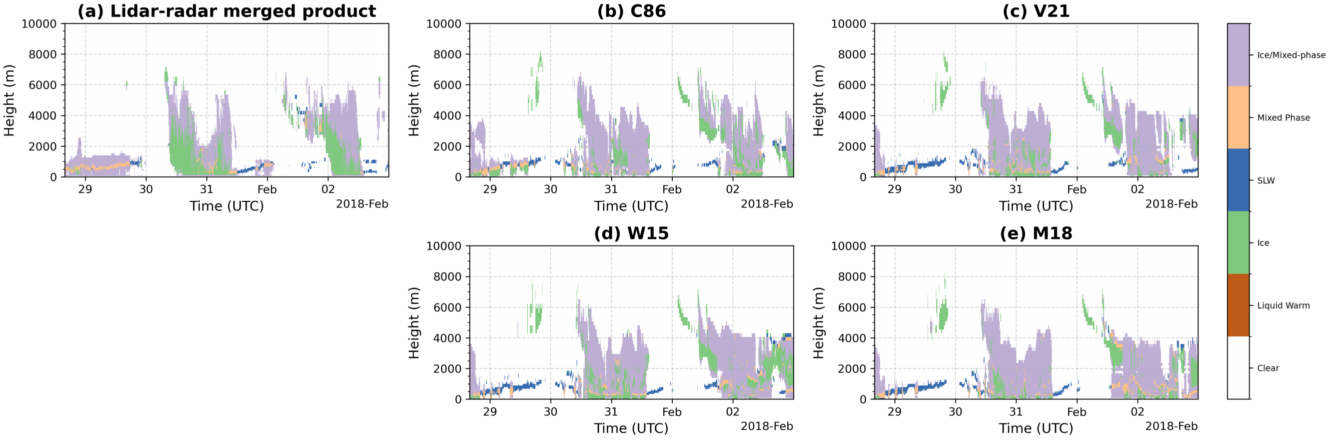

Figure 4. Time-height cross-sections of the cloud phase derived from the **(a)** merged lidar-radar product and the **(b-e)** corresponding forward simulated phase masks from the four model configurations using the EMC^2 simulator.

surface during the first phase of the SLW period and both phases of the MIX period, which align closely with periods of strong surface winds (Figure A2a, Figure A1g). The TOC mass concentration is generally lower than SSA in the boundary layer but also shows wind-driven enhancements, alongside some noticeable free-tropospheric intrusion from aloft (Figure A2b).

The observed INP concentrations generally fall between the simulations of the two dynamical schemes. The W15 scheme overestimates the INP concentrations by up to 2 orders of magnitude around $-22\,^{\circ}\mathrm{C}$, while the M18 scheme underestimates them by up to 2 orders of magnitude around $-28\,^{\circ}\mathrm{C}$ and $-15\,^{\circ}\mathrm{C}$. Overall, this indicates a consistent 1 to 2 order of magnitude difference in the predicted INP concentrations between the W15 and M18 parametrizations (Figure 3).

3.3 Cloud Phase and Hydrometeor Response

With the pronounced differences in INP concentrations demonstrated in the previous section, we now investigate how these parametrizations modulate the macroscopic cloud phase partitioning. To ensure a physically consistent and direct comparison with the observations, the (EMC^2) simulator was applied to the high-frequency model outputs. Figure 4 presents the time-height cross-sections of the cloud phase derived from the ship-based merged lidar-radar product as previously shown in Figure 2, alongside the simulated cloud phase masks from the four model configurations.

During the SLW periods, the C86 configuration reproduces fewer SLW clouds than observed (Figure 4b). In the first phase of the SLW period from late 28 January to end of 29 January, C86 simulates shallower, less consistent mixed-phase layers compared to the observations and erroneously produces precipitating ice beneath the mixed-phase layer, a feature absent in the observations (Figure 4a, b). Similarly, in the second SLW period following the deep convective ice clouds in late 31 January, C86 fails to reproduce the prolonged SLW layers seen in the observations (Figure 4a, b). The three other configurations with substantially lower INP concentrations than C86 (Figure 3), simulate more persistent SLW layers (Figure 4c, d, e). In the first SLW phase, these configurations generate SLW layers with less underlying precipitating ice, better aligning with observations,

https://doi.org/10.5194/egusphere-2026-3541
Preprint. Discussion started: 9 July 2026
© Author(s) 2026. CC BY 4.0 License.

although they underestimate the presence of ice crystals within the shallow SLW layer (Figure 4a, c, d, e). In the second SLW phase, V21, W15, and M18 produce SLW layers that are more comparable to the observations.

The cloud structures during MIX period is more complex and the response of the cloud phase to INP variations differs considerably. While the general cloud structure such as the cloud top height and its temporal evolution is captured by all model configurations, the phase partitioning within the deep clouds varies (Figure 4). Notably, all configurations underestimate the total ice occurrence during both phases of the MIX period compared to the observations (Figure 4). The V21 and W15 configurations exhibit an increase in mixed-phase clouds during the first MIX period from mid-30 to mid-31 January (Figure 4c, d). In the second MIX period, W15 and M18 simulate prolonged deep mixed-phase clouds at the end of 2 February, which is absent in the observations (Figure 4a, d, e).

The hydrometeor mass mixing ratio is examined to understand the drivers for the cloud phase changes. Figure 5 depicts the time-height cross-sections of five hydrometeor species: cloud liquid, rain, ice, snow, and graupel. The first row displays the absolute mass mixing ratios for the C86 configuration, while the subsequent rows illustrate the differences between the other configurations and C86. The microphysical changes in V21 and W15 are similar, characterized by fluctuating but overall increased cloud liquid, rain, and graupel masses (Figure 5f, g, j, k, l, o), accompanied by a general decrease in snow mass (Figure 5i, n). The ice crystal mass exhibits a subtle decreasing trend in the boundary layer but increases in the lower free troposphere around 4 to 6 km (Figure 5h, m). For the M18 configuration, the trends in hydrometeor mass changes are qualitatively similar to V21 and W15 but are significantly larger in magnitude, producing substantially more liquid, rain, and graupel, alongside a more consistent and pronounced reduction in both ice and snow mass (Figure 5p-t).

These microphysical changes profoundly impact the column-integrated water paths. Figure 6 presents the timeseries of the observed and simulated LWP and IWP, with corresponding statistical boxplots separated by the cloud regimes. A quantitative summary of the mean and median values of LWP and IWP in observations and model configurations is provided in Table 1. The observations reveal a significantly higher LWP during the SLW period compared to the MIX period, with mean values of approximately 192.14 $\mathrm{g\,m^{-2}}$ versus 70.04 $\mathrm{g\,m^{-2}}$, respectively (Figure 6a, b; Table 1). The observed IWP is negligible during the SLW period (mean $\sim 1.18\,\mathrm{g\,m^{-2}}$) but is clearly present during the MIX period, generally not exceeding 200 $\mathrm{g\,m^{-2}}$ with a mean of $23.14\,\mathrm{g\,m^{-2}}$ (Figure 6c, d; Table 1).

Regarding model performance, the C86 consistently underestimates LWP throughout the case study. During the SLW period, V21, W15, and M18 simulate comparable amounts of LWP to C86 with means ranging from 35.32 to $43.29\,\mathrm{g\,m^{-2}}$, all exhibiting a substantial underestimation of liquid water (Figure 6a, b; Table 1). Nevertheless, during the MIX periods, the three configurations with reduced INP concentrations demonstrates a pronounced enhancement in SLW. While the C86 scheme depletes a lot liquid water with mean LWP of $19.33\,\mathrm{g\,m^{-2}}$, the V21 and W15 schemes moderately increase the mean LWP to 29.32 and $34.73\,\mathrm{g\,m^{-2}}$ respectively (Table 1). The M18 configuration, in particular, exhibits a massive enhancement in LWP with a mean of $129.57\,\mathrm{g\,m^{-2}}$ (Table 1). Unlike C86, the V21, W15, and M18 are able to simulate the LWP spike observed in early 30 January and generally increase liquid water during both phases of the MIX period, although M18 appears to overestimate the magnitude of the LWP (Figure 6a, b).

© Author(s) 2026. CC BY 4.0 License.

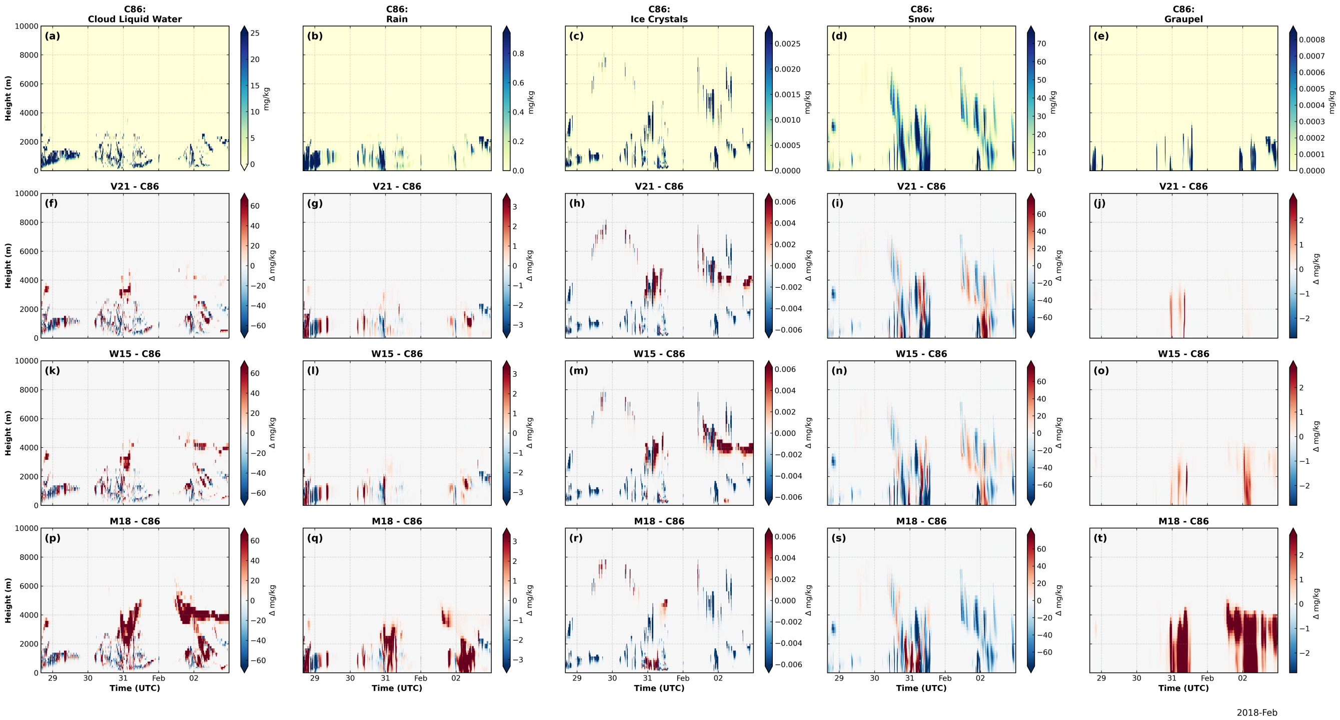

Figure 5. Time-height cross-sections of the simulated hydrometeor mass mixing ratios along the ship track. The columns represent cloud liquid water, rain, ice crystals, snow, and graupel. The top row displays the absolute mass mixing ratios ($\mathrm{mg\,kg^{-1}}$) for the default C86 configuration. The subsequent rows display the differences ($\Delta\mathrm{mg\,kg^{-1}}$) between the other configurations (V21, W15, M18) and the C86.

Table 1. Mean and Median Values of LWP and IWP in the SLW and MIX periods for Observations and Model Configurations

	Liquid Water Path [g $\mathrm{m^{-2}}$]				Ice Water Path [g $\mathrm{m^{-2}}$]			
	SLW		MIX		SLW		MIX	
	Mean	Median	Mean	Median	Mean	Median	Mean	Median
CAPRICORN-2	192.14	173.00	70.04	62.00	1.18	0.18	23.14	8.94
C86	35.32	16.47	19.33	7.16	20.44	1.00	111.09	64.37
V21	42.23	15.72	29.32	19.29	**4.02**	**0.02**	85.86	29.32
W15	39.15	15.08	**34.73**	19.17	8.71	**0.02**	**74.82**	34.98
M18	**43.29**	**21.27**	129.57	**96.56**	6.32	0.01	108.51	**24.49**

Note. Bold values denote the closest agreement with observations.

For the simulation of IWP, all model configurations correctly simulate near-zero median IWP during the SLW periods, aligning well with the observation (Figure 6c, d; Table 1). During the MIX periods, all configurations produce significantly

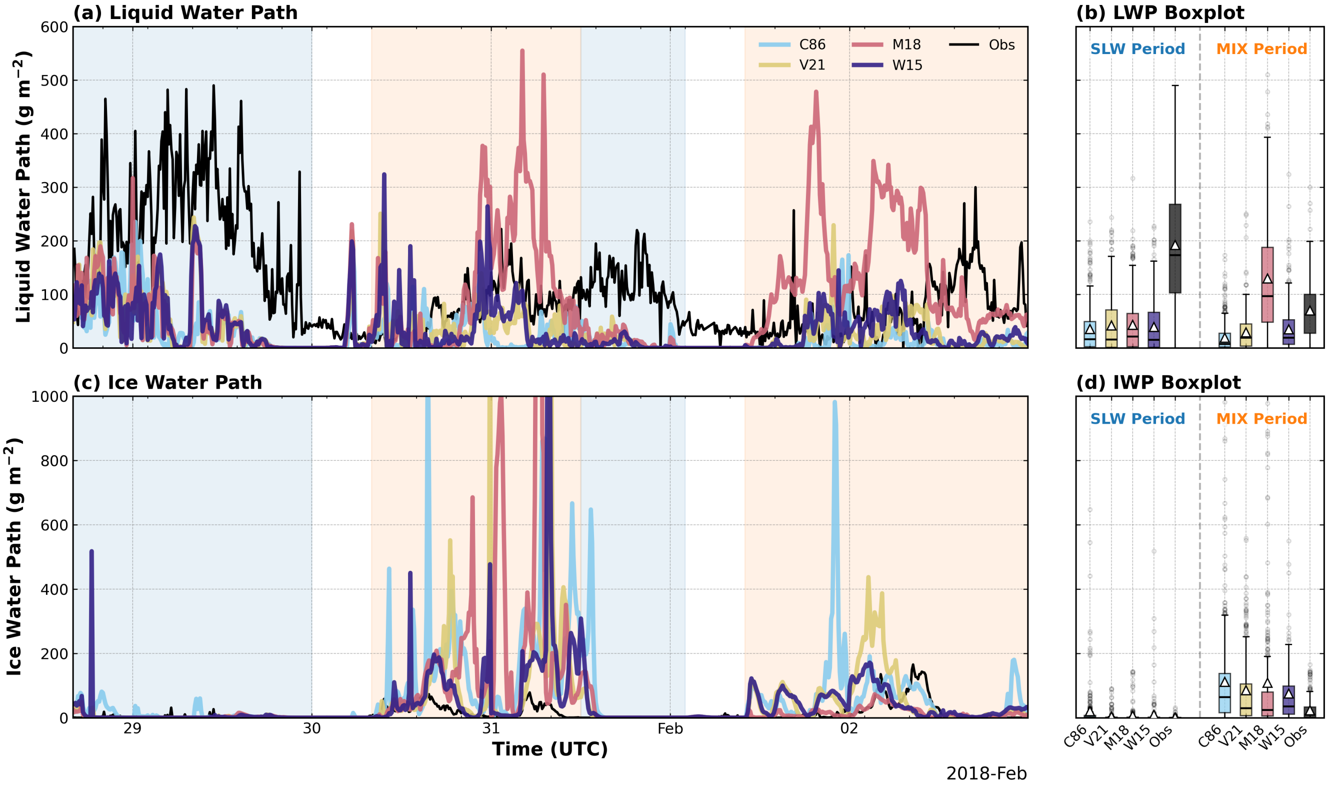

Figure 6. (a, c) Timeseries of the LWP and IWP simulated by the model configurations compared against the shipborne microwave radiometer and radar-derived retrievals (black lines), respectively. The light blue and light orange background shadings denote the SLW and MIX periods. **(b, d)** Statistical boxplots of the LWP and IWP grouped by the two distinct cloud regimes. In the boxplots, the boxes represent the interquartile range (IQR, 25th to 75th percentiles), the central horizontal line indicates the median, and the white triangle marks the mean value. The circles denote outliers.

higher IWP, including several spurious high value spikes during the first phase of the MIX period. Statistically, while the V21, W15, and M18 configurations successfully reduce the mean and median IWP values compared to C86, they still tend to overestimate the total IWP relative to the observations (Figure 6d; Table 1).

3.4 Thermodynamic Evaluation against Radiosonde

To further elucidate the physical mechanisms driving the regime-dependent cloud phase responses to different INP schemes, we evaluate the vertical thermodynamic structures using radiosonde profiles. Figure 7 presents the vertical profiles of air temperature, relative humidity over water (RH_w), and relative humidity over ice (RH_i) along with mean cloud top and base height, separated into the SLW and MIX periods.

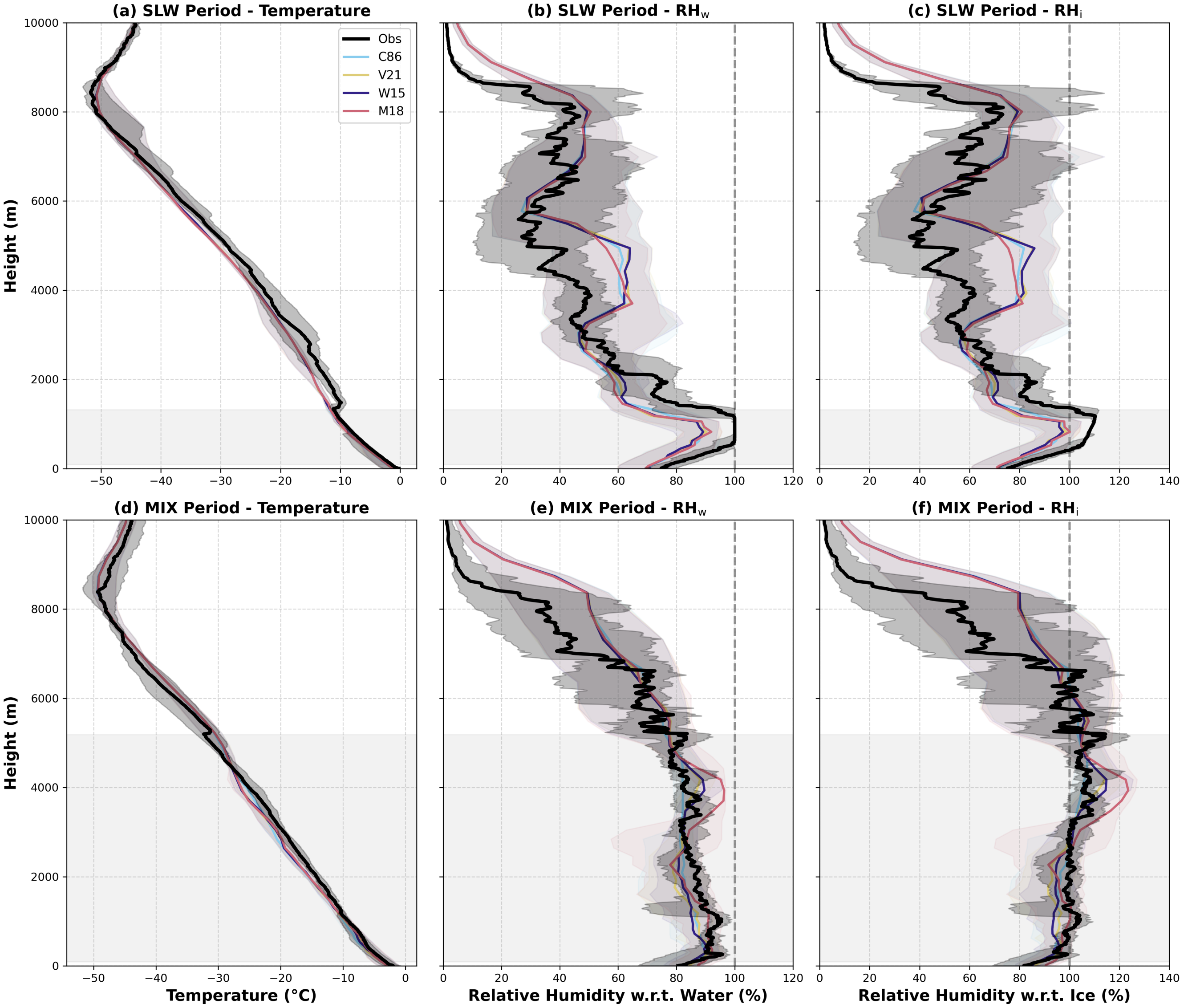

Figure 7. Vertical profiles of thermodynamic structures evaluated against radiosonde measurements. Panels **(a)**, **(b)**, and **(c)** present the profiles of air temperature, relative humidity over water, and relative humidity over ice during the shallow SLW periods, respectively. Panels **(d)**, **(e)**, and **(f)** present the corresponding profiles during the deep MIX periods. Solid lines represent the median profiles for the observations (black) and the model configurations (colored). The surrounding shadings denote the 25th to 75th interquartile ranges. The grey horizontal bands in the background approximate the mean vertical extent of the cloud layers during each regime, as determined by the lidar-radar cloud phase observations. The 100% saturation threshold is marked by vertical dashed lines in the humidity plots. Observational statistics are based on 14 radiosondes during the SLW period and 12 during the MIX period, whereas model statistics incorporate all available outputs within each respective period.

During the SLW periods, the observations indicate a mean cloud top height of approximately 1.3 km, corresponding to a cloud top temperature of around $-10\,^{\circ}\mathrm{C}$ (Figure 7a). A pronounced temperature inversion is observed capping the cloud layer, a characteristics feature of marine boundary layer stratocumulus. Nevertheless, all model configurations consistently fail to represent this sharp inversion at the cloud top (Figure 7a). Above the cloud layer up to an altitude of around 8 km, all configurations exhibit slightly underestimated temperatures compared to the radiosonde data (Figure 7a). The impact of this missing inversion is reflected in the RH profiles. Within the shallow cloud layer, the observed RH_w reaches 100% (Figure 7b), coinciding with an ice supersaturation (Figure 7c), charasteristic of these supercooled environments. In contrast, all model configurations systematically underestimate the boundary layer moisture, failing to reach water saturation and barely reaching ice saturation. Above the cloud top, the humidity variability broadens significantly. The models generally underestimate moisture below 3 km and subsequently overestimate it at higher altitudes (Figure 7b, c). The differences among the microphysics configurations in this shallow regime are minimal, though W15 exhibits a marginal improvement in simulated RH between 1.5 and 2.2 km, and M18 shows a slight improvement between 4 and 5.5 km (Figure 7b, c).

Regarding the MIX periods, the radiosonde observations reveal a subtle temperature inversion occurring near the mean cloud top at approximately 5.2 km, although this feature is less distinct within the 25th and 75th percentile bounds (Figure 7d). The simulated temperature profiles across all model configurations perform generally well, with their ranges aligning closely with the observations throughout the troposphere. Humidity exhibits more variance in both observations and model configurations. Within the lower section of the deep cloud layers (below 2 km), the M18 configuration yields improved RH_w and RH_i that better align with the observations, whereas the other configurations exhibit dry biases (Figure 7e, f). Conversely, from 2 km up to the cloud top, M18 produces excessive humidity compared to both observations and the other configurations (Figure 7d, e). Above the cloud top and into the upper troposphere, all model configurations demonstrate a tendency to reproduce more humidity than observed during the MIX period.

3.5 Surface Radiative Fluxes Evaluation

The microphysical responses to INP concentrations ultimately affect the surface radiative fluxes. Figure 8 displays the time-series and statistical boxplots of the simulated and observed downwelling surface SW and LW fluxes. A quantitative summary of the mean and median radiative fluxes in observations and model configurations is provided in Table 2. The radiative performance of each model configuration directly reflects its ability to simulate the LWP within the respective cloud regimes.

During the shallow SLW periods, observations show low downwelling SW fluxes, remaining mostly below $200\,\mathrm{W\,m^{-2}}$ on 29 January and reduced compared to the clear-sky period on 30 January and 1 February (Figure 8a). This coincides with high downwelling LW fluxes of approximately $300\,\mathrm{W\,m^{-2}}$ (Figure 8b). All model configurations struggle during these SLW periods, strongly overestimating SW radiation and underestimating LW radiation. All configurations simulate overestimated SW fluxes exceeding $210\,\mathrm{W\,m^{-2}}$ compared to a mean value of $70.76\,\mathrm{W\,m^{-2}}$ in observations (Table 2). The observed mean LW flux of $293.1\,\mathrm{W\,m^{-2}}$ is severely underestimated by approximately 35 to $40\,\mathrm{W\,m^{-2}}$ across all runs. The boxplots for the SLW period (Figure 8c, d) confirm this performance. The flux distributions from C86, V21, W15, and M18 are nearly identical,

https://doi.org/10.5194/egusphere-2026-3541
Preprint. Discussion started: 9 July 2026
© Author(s) 2026. CC BY 4.0 License.

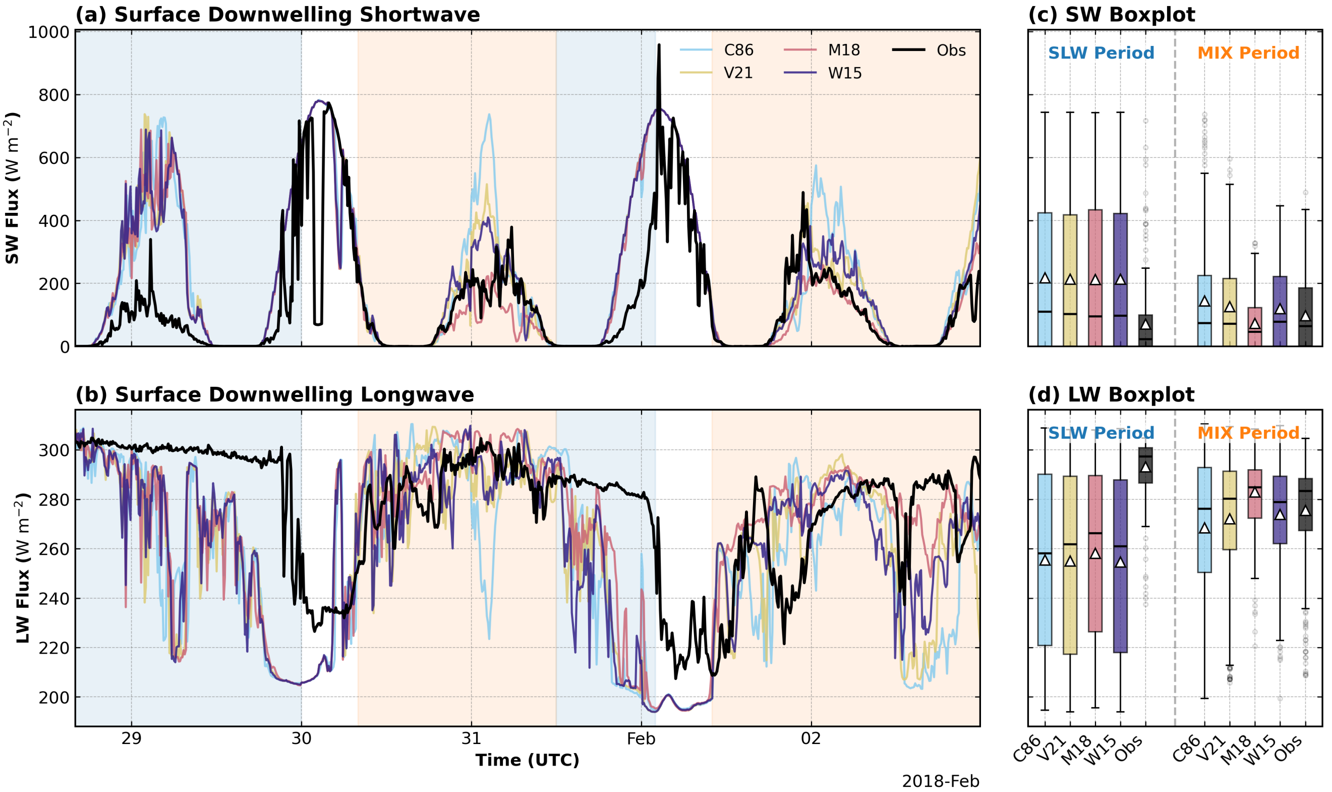

Figure 8. (a, b) Timeseries of the downwelling surface shortwave and longwave radiation fluxes simulated by the model configurations compared against shipborne pyranometer and pyrgeometer measurements (black lines). The light blue and light orange background shadings denote the SLW and MIX periods, respectively. **(c, d)** Statistical boxplots of the SW and LW fluxes grouped by the two distinct cloud regimes. The boxplot conventions are identical to those described in Figure 6.

showing only minimal improvement from the schemes with reduced INP concentrations and enhanced LWP, and all remain clearly separated from the observational distributions.

During the MIX periods, the differences among the model configurations become pronounced. On 31 January and 2 February, C86 simulates the highest downwelling SW fluxes, with midday peaks reaching $700\,\mathrm{W\,m^{-2}}$ and $580\,\mathrm{W\,m^{-2}}$, respectively (Figure 8a). This yields a substantially overestimated mean SW flux of $144.34\,\mathrm{W\,m^{-2}}$ compared to the observed $96.92\,\mathrm{W\,m^{-2}}$ (Table 2). In contrast, V21, W15, and M18 simulate notably lower SW peaks, aligning more closely with the observed magnitudes. The SW boxplots for the MIX period (Figure 8c) and Table 2 quantitatively demonstrate this in which the mean and median SW values for V21, W15, and M18 are markedly reduced compared to C86. Specifically, M18 produces the lowest overall SW distribution, shifting the mean to $72.94\,\mathrm{W\,m^{-2}}$ and the median to $46.30\,\mathrm{W\,m^{-2}}$, which slightly overcorrects the positive bias and yields SW fluxes lower than the observations. For downwelling LW fluxes, C86 generally simulates the lowest values, particularly on 31 January and early 2 February (Figure 8b), resulting in a mean LW flux of $268.38\,\mathrm{W\,m^{-2}}$ versus the

Table 2. Mean and Median Values of Downwelling SW and LW Fluxes in the SLW and MIX periods for Observations and Model Configurations

	Downwelling Surface SW flux [W m^{-2}]				Downwelling Surface LW flux [W m^{-2}]			
	SLW		MIX		SLW		MIX	
	Mean	Median	Mean	Median	Mean	Median	Mean	Median
CAPRICORN-2	70.76	22.30	96.92	64.15	293.10	297.30	275.48	283.30
C86	217.37	110.15	144.34	73.51	255.35	258.13	268.38	276.09
V21	213.30	102.25	125.51	**72.00**	255.06	261.80	272.14	280.27
W15	213.45	97.62	**119.01**	77.90	254.63	260.91	**273.86**	278.80
M18	**212.17**	**94.91**	72.94	46.30	**258.11**	**266.19**	282.92	**284.84**

Note. Bold values denote the closest agreement with observations.

observed $275.48\,\mathrm{W\,m^{-2}}$ (Table 2). V21, W15, and M18 produce higher LW fluxes during these MIX phases, reducing the negative LW bias. The boxplots (Figure 8d) and statistical means (Table 2) confirm that V21, W15, and M18 shift the LW distribution upward compared to C86. The M18 configuration yields a median LW flux of $284.84\,\mathrm{W\,m^{-2}}$, which is the most comparable to the radiometer measurements of $283.30\,\mathrm{W\,m^{-2}}$. Overall, while differences among the schemes are negligible during the SLW periods, V21, W15, and M18 clearly reduce both the SW overestimation and the LW underestimation during the MIX periods, even though M18 slightly overcorrects these biases.

To expand our evaluation beyond the single-point ship trajectory, we examine the spatial influence of the INP parametrizations on the domain-wide downwelling surface SW fluxes. Figure 9 illustrates the spatial distribution of surface SW fluxes associated with MSLP contours for the four model configurations, capturing a representative snapshot during the SLW period (29 January, 00:30 UTC, left column) and the MIX period (02 February, 03:00 UTC, right column). In these greyscale maps, whiter shading indicates lower SW fluxes reaching the surface, corresponding to optically thicker and more reflective clouds. During the SLW period (left column), the broad post-frontal stratocumulus cloud west of the low-pressure system shows consistent SW transmission across all model configurations. Specifically, the spatial distribution and magnitude of SW fluxes near the ship (yellow star) are essentially identical across the schemes. Nevertheless, in the area further west (near 62°S–65°S, 130°E–135°E), cloud optical thickness visibly increases denoted by brighter shading in the three low INP runs, with the most pronounced effect in M18. The spatial influence of the INP parametrizations on deep frontal clouds becomes highly pronounced during the MIX period (right column), when SW transmission through the frontal band is substantially reduced is increased substantially in V21, W15, and M18 compared to C86 scheme (Figure 9).

© Author(s) 2026. CC BY 4.0 License.

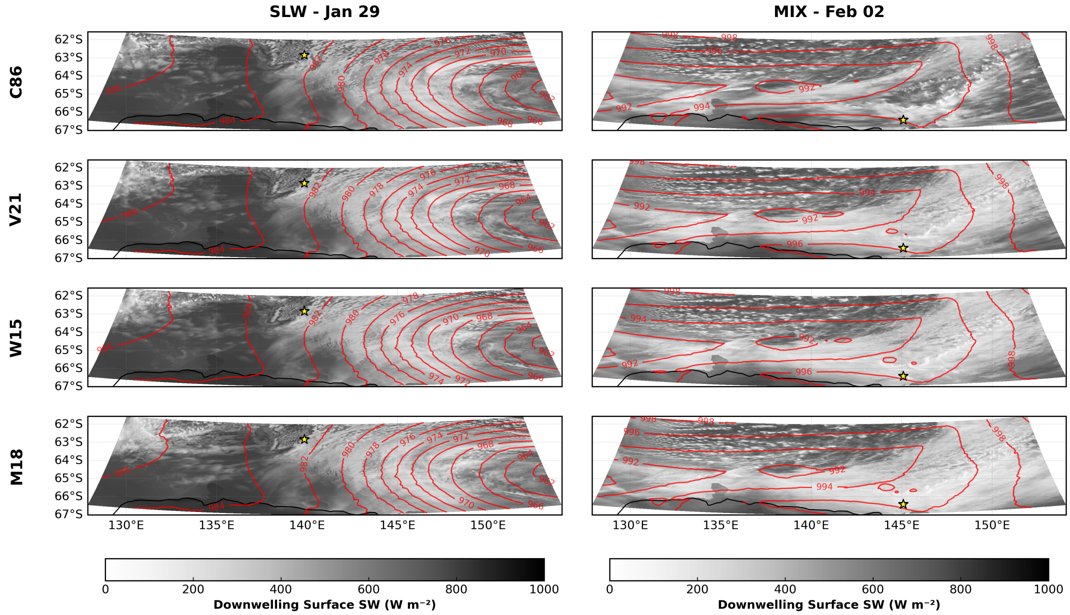

Figure 9. Spatial distributions of downwelling surface shortwave radiation fluxes overlaid with mean sea level pressure contours (red lines, in hPa) for the four model configurations. The left column represents a snapshot during the post-frontal SLW period at 03:00 UTC on 29 January. The right column captures a snapshot during the deep MIX period at 03:00 UTC on 02 February. The greyscale shading indicates the magnitude of the downwelling SW fluxes ($\mathrm{W\,m^{-2}}$). The yellow star denotes the location of the RV *Investigator*.

4 Discussions

The results presented in Section 3 provide key insights into UM simulations of mixed-phase clouds across different synoptic regimes during a high-latitude SO case study, highlighting their microphysical and radiative sensitivities to altered INP parametrizations.

4.1 INP representations

In this study, we introduced two aerosol-aware diagnostic INP parametrizations (W15 and M18) coupled to the prognostic emissions of TOC and SSA from the GLOMAP-mode scheme. Comparisons with shipborne measurements demonstrate that these dynamical schemes agree significantly better with observations than the C86 scheme (Fig. 3). However, the simulated INP magnitudes are not perfectly represented. The W15 scheme tends to slightly overestimate, while the M18 scheme slightly underestimates the observed concentrations (Fig. 3). Besides the prerequisite of correctly simulating the basic atmospheric thermodynamic conditions such as temperature and moisture profiles needed to form clouds in the first place, accurately representing INPs in models fundamentally relies on two pillars: predicting the correct aerosol source and applying the correct parametrization. We discuss the uncertainties associated with both aspects below, followed by an assessment of the missing role of mineral dust.

https://doi.org/10.5194/egusphere-2026-3541
Preprint. Discussion started: 9 July 2026
© Author(s) 2026. CC BY 4.0 License.

4.1.1 Uncertainties in Aerosol Sources

For the M18 parametrization, predicted INP concentrations are directly proportional to the surface area of SSA in the soluble accumulation and coarse mode. In GLOMAP, SSA emission follows Gong (2003), which calculates the sea salt flux as a function of the 10-m wind speed and a prescribed size distribution. Nevertheless, several weaknesses of this parametrization have been investigated by recent studies. Primarily, it neglects the important impact of sea surface temperature (SST). As demonstrated by Jaeglé et al. (2011) and Salter et al. (2015), the kinematic viscosity of seawater increases substantially at the near-freezing temperatures typical of the SO. This elevated viscosity slows bubble rise velocities and alters the surface bubble size spectrum, effectively suppressing jet drop formation and significantly reducing the emission of supermicron sea spray aerosols. Furthermore, applying the Gong (2003) scheme to extreme wind conditions presents another challenge. During the deep frontal passages in our case study, surface wind gusts reached $15\,\mathrm{m\,s^{-1}}$ (Fig. A1g). Observational constraints suggest that at such high wind speeds, the SSA emission flux does not continue to increase exponentially, but begins to level off due to complex wave-breaking and spume generation dynamics (Revell et al., 2019). Utilizing perturbed parameter ensembles (PPEs) in the UK Hadley Centre General Environment Model (HadGEM3), Regayre et al. (2020) revealed that sea spray emissions in the model need to be significantly higher than those calculated by Gong (2003) in the austral summer of the SO when the wind speed is relatively low. Consequently, constraining SSA fluxes to realistic values across varying synoptic states is a highly complex process, directly impacting the accuracy of the INP concentrations predicted by M18.

For the W15 parametrization, INP concentrations scale with the simulated mass of TOC. In our configuration, PMOA emissions are parametrized using the Gantt et al. (2011, 2012) scheme, which relies on surface wind speed and ocean chlorophyll-a (Chl-a) concentrations as a proxy for biological productivity. Subsequently the PMOA flux to the air is calculated relying on SSA emissions. The uncertainties in SSA emissions that we discussed above will propagate into the PMOA emission. Another uncertainty arises from the Chl-a concentrations. GLOMAP-mode currently utilizes a monthly Chl-a climatology derived from the GlobColour satellite dataset (Garnesson et al., 2019). The coarse temporal resolution fundamentally lacks the synoptic variability required to capture rapid biogeochemical responses to frontal passages, and its validity over the SO is heavily hindered by cloud cover. Furthermore, conventional satellite algorithms rely on global assumptions linking chlorophyll-a to total phytoplankton biomass, which often are not representative in the SO. Local phytoplankton species behave differently, exhibiting unique physiological adaptations that alter their cellular chlorophyll content, thereby complicating the estimation of actual biological productivity (Haëntjens et al., 2017). Transitioning to coupled atmosphere-ocean biogeochemical models has been strongly advocated for to represent realistic fluxes of marine biogenic precursors, which is critical not only for PMOA but also for estimating dimethyl sulfide (DMS) emissions, a key CCN source over the SO (Vergara-Temprado et al., 2017; Mallet et al., 2023). Beyond the dataset limitations, the validity of using Chl-a as a proxy for PMOA has itself been questioned by Russell et al. (2023), suggesting that Chl-a may not be a reliable general proxy for marine organics. Moreover, the assumption that all PMOA is released into the Aitken mode may oversimplify the emission process (Quinn et al., 2015; Prather et al., 2013). Additionally,we excludes the contribution of the insoluble Aitken mode OM in this study to account for calculation of immersion freezing INP. As freshly emitted insoluble particles gradually transition into soluble modes and grow into the accumulation mode through atmospheric aging and coagulation, this exclusion inherently provides a conservative, lower-bound estimate of the TOC mass, potentially contributing to the slight underestimations of INPs by W15.

4.1.2 Uncertainties in the Parametrizations

Beyond the prognostic aerosol sources, the formulations of the M18 and W15 schemes introduce inherent limitations when applied to the pristine SO. For M18, active site density (n_s) function was derived from a single North Atlantic coastal site, meaning its application to the open-ocean conditions of the SO remains unverified. Consequently, this study serves as an initial, albeit also limited, verification of its performance in this region. Moreover, M18 focuses on heat-stable organic coatings, completely ignoring heat-labile marine microbes, which typically dominate the INP population at temperatures warmer than $-20\,^{\circ}$C. In addition, as SSA is acting as a proxy for PMOA in M18 parametrization, the performance of M18 is heavily tied to the SSA surface area. In this study, only soluble accumulation and coarse mode SSA were considered, as Aitken mode SSA is not yet incorporated into the GLOMAP-mode prognostic fields, further constraining the available INP surface area.

Regarding the W15 parametrization, the scheme exhibits critical physical and mathematical limitations. Physically, it assumes that the ocean SML has the same ice-nucleating properties as the SSA in the air, ignoring the bubble-bursting process that selects certain chemicals over others when emitting aerosols into the atmosphere (Burrows et al., 2013). Mathematically, the scheme relies on a singular approximation ($\lambda < 0.1$) which may not work for coarse particles or at temperatures below $-27\,^{\circ}$C (Vergara-Temprado et al., 2017). By failing to account for the probability that multiple active sites may reside within a single droplet, the W15 scheme assumes each site initiates freezing in a separate droplet. Therefore, the model overestimates the fraction of frozen droplets and the resulting primary ice crystal number. Consequently, global models using W15 systematically overpredict INP concentrations in mixed-phase clouds (McCluskey et al., 2019). These inherent biases corroborate our findings that W15 reproduces slightly higher INP concentrations than the observations (Fig. 3). Biogeochemically, the W15 formulation was derived from a generalized global distribution of SML samples, which poorly represents the unique environment of the high-latitude SO. As highlighted by Mallet et al. (2023), the phytoplankton communities along the Antarctic coast produce organic materials with very different ice-nucleating properties compared to those found in warmer waters. Together, the uncertainties in both the aerosol sources and the parametrization equations highlight the challenge to accurately represent marine organic aerosols as INPs in pristine polar environments.

4.1.3 The Role of Mineral Dust INPs in the High-Latitude SO

While this study focuses on marine-sourced INPs, the contribution of mineral dust to the global INP budget cannot be ignored. Mineral dust, particularly potassium feldspar, is recognized as the most abundant and efficient source of heterogeneous INP globally (Hoose and Möhler, 2012; Kanji et al., 2017). Although the SO and coastal Antarctica have generally pristine marine boundary layers, terrestrial aerosols can be transported to this region. Recent aircraft observations during the Southern Ocean Cloud Radiation and Aerosol Transport Experimental Study (SOCRATES) campaign detected mineral dust within ice crystals over the SO, confirming their active role in cloud glaciation (Twohy et al., 2021). Global modelling studies further demonstrate a temperature-dependent shift in INP populations over this region (Vergara-Temprado et al., 2017; McCluskey et al., 2023).

© Author(s) 2026. CC BY 4.0 License.

Marine aerosols dominate at warmer supercooled temperatures above $> -20\,^{\circ}\mathrm{C}$, whereas long-range transported dust from continents governs the INP budget at temperatures below $-25\,^{\circ}\mathrm{C}$.

During the MIX periods in our case study, deep frontal cloud tops frequently cooled below $-30\,^{\circ}\mathrm{C}$ (Fig. 7). By applying only marine-sourced INP schemes, our simulations neglect the contribution of these highly efficient refractory dust particles in the upper troposphere. As Herbert et al. (2025) pointed out, capturing INP concentrations in Antarctic airmasses requires accurate global dust distributions. The absence of a dust INP parametrization likely explains why M18 and W15, despite their fidelity in the lower troposphere, might underestimate ice formation at the cold cloud tops. Therefore, future simulations over the SO need to combine dynamic marine schemes with dust parametrizations to fully close the INP budget across the entire mixed-phase temperature ranges.

4.2 Regime-dependent response of cloud radiative properties to INP parametrizations

Having discussed the uncertainties within aerosol-aware INP parametrizations, we now investigate the influence of these distinct INP schemes on cloud properties and surface radiation fluxes.

Overall, with closer agreement with observed INP concentrations, the V21, W15, and M18 schemes suppress cloud glaciation. This leads to longer lasting SLW clouds (Figure 4), enhanced LWP (Figure 6), and reduced surface SW in conjunction with enhanced LW radiative fluxes (Figure 8), presenting better agreement with observations. Our findings are strongly corroborated by recent modelling studies targeting the SO and Antarctic coast. Vergara-Temprado et al. (2018) demonstrated that replacing high concentration continental INP schemes with marine-specific parametrizations substantially mitigated the over-glaciation bias, allowing for robust increases in LWP and significant improvements in reflected SW radiation in the UM. Similarly, implementing the observationally tuned V21 scheme in the Weather Research and Forecasting (WRF) model has been shown to maintain SLW layers and reduce positive surface SW biases over the Antarctic coast (Vignon et al., 2021; Hines et al., 2021). Consistent with these studies, our results confirm that resolving the radiation bias fundamentally requires models to capture the low INP concentrations typical of the pristine SO.

A critical finding of our study is that the response of cloud phase, LWP, and radiative fluxes to altered INP concentrations is strongly dependent on the synoptic regime. In the post-frontal shallow stratocumulus-dominated cloud regime, the effect of altering INP parametrizations is negligible, resulting in a persistent and severe underestimation of LWP and overestimation of surface SW fluxes across all configurations (Figure 6 and Figure 8). However, during the deep convective mixed-phase cloud regimes driven by frontal passage, we observe significant improvements in LWP and radiations. This suggests that other factors dominate the simulation of boundary layer stratocumulus clouds under post-frontal conditions.

A primary driver of this microphysical insensitivity appears to be the misrepresentation of the boundary layer inversion strength and the moisture abundance. As shown in Figure 7a and b, all model configurations fail to reproduce the sharp temperature inversion at cloud top around 1.3 km and the associated boundary layer moisture during the post-frontal SLW periods. Bodas-Salcedo et al. (2014, 2016) revealed that SO radiative biases originated predominantly from low- and mid-level clouds in the post-frontal sectors of extratropical cyclones. The representation of capping inversions in these regions has been a challenge for numerical models for a long time. Huang et al. (2014) pointed out that models generally represent large-scale driven frontal clouds well, but struggle significantly with widespread post-frontal boundary layer clouds. They attributed this to weak simulated temperature inversion strength which result in overestimated entrainment that mixes dry free-tropospheric air into the boundary layer, inhibiting SLW maintenance. Furthermore, Vignon et al. (2021) investigated the factors controlling SLW over coastal Antarctica, suggesting that while tailored INP parametrizations and higher vertical resolution improve SLW simulations, the turbulence parametrization controlling cloud-top mixing plays an equally critical role. Underestimated turbulent mixing can prematurely deplete SLW, indicating that developing non-local turbulent mixing parametrizations based on mass-flux schemes may be a necessary future step (Vignon et al., 2021). Therefore, boundary layer dynamics, including surface fluxes, turbulence, wind shear, entrainment, and large-scale subsidence, fundamentally regulate the maintenance of low-level SLW clouds in post-frontal environments.

An additional cause for the insensitivity of cloud and radiation to INP concentrations during the SLW period may arise from the model evaluation approach in this study. Conducting point-to-point comparisons by interpolating model outputs to the ship's location limits perspective of the broader domain. Figure 9 confirms this limitation, showing that although surface SW fluxes at the ship's exact location do not vary significantly across configurations during the SLW period, distinct differences in cloud reflectivity emerge in the western sector of the domain. This highlights the inherent limitations of evaluating high-resolution models solely against a single shipborne case study. Furthermore, apart from microphysical properties, another major source of uncertainty modulating surface radiative fluxes is the macroscopic cloud fraction. Since traditional vertically pointing shipborne sensors cannot fully capture the spatial distribution of clouds, future observational campaigns should prioritize the deployment of scanning instruments. Such measurements would allow for the direct retrieval of spatial cloud fraction, enabling more robust comparisons with the cloud fraction simulated by the model.

Moreover, a supplementary sensitivity test with INP concentrations set to near-zero (not shown) exhibited slightly further increased LWP during the MIX periods, but produced no change during the SLW periods. Modifying the INP parameterization can only increase SLW by reducing glaciation but can't generate more liquid water through droplet activation processes. Therefore, the insensitivity during the SLW period indicates that the lack of simulated liquid water is primarily driven by a profound lack of moisture in the boundary layer as a first-order problem, with the phase partitioning of the cloud being a secondary issue. This directs attention to the large-scale forcing provided by the model's initialization and lateral boundary conditions. If the advected air masses lack sufficient moisture from the beginning, no microphysical adjustment can enhance the LWP. Additionally, the MSLP in all model configurations present consistent overestimation compared to observations (Appendix Figure A1e), indicating that the initial and boundary conditions has systematically underestimated the intensity of the cyclone, leading to weakened large-scale updrafts and underestimated moisture transport from the subtropics, even when the driving model is nudged with ERA5 reanalysis. As recently demonstrated by Price et al. (2025), utilizing more realistic meteorological boundary fields can significantly alleviate biases in the UM. Our findings during the SLW period corroborate this conclusion, emphasizing that resolving SO cloud biases requires an improvement of both model physics and the fidelity of the large-scale meteorological forcing.

https://doi.org/10.5194/egusphere-2026-3541
Preprint. Discussion started: 9 July 2026
© Author(s) 2026. CC BY 4.0 License.

5 Conclusions and Outlooks

In this study, we evaluated the sensitivity of cloud and radiation properties to different INP parametrizations using the UM RAL3 high-resolution regional model, coupled with CASIM cloud microphysics and GLOMAP-mode aerosol schemes. Simulations were compared against comprehensive shipborne observations from the CAPRICORN-2 campaign over the high latitude SO. We presented the first online implementation of aerosol-aware deterministic INP schemes in a high-resolution regional configuration, driven directly by prognostic sea spray and marine organic aerosol fields. Model performance was assessed during a period of strong cyclonic and biological activity, which was partitioned into two distinct cloud regimes: a post-frontal shallow SLW period and a frontal deep mixed-phase period.

The default C86 scheme severely overestimates INP concentrations over the SO by 2 to 4 orders of magnitude compared to observations. This leads to over-glaciation of mixed-phase clouds, resulting in a significant underestimation of LWP and overestimation of downwelling surface SW radiation. The V21 scheme tailored to the coastal Antarctic environment successfully captures the low INP concentrations and improves cloud and radiation simulations. Given its low computational cost and robust performance over the SO and Antarctic coast, V21 represents a highly practical INP parametrization for operational weather forecasting in these regions. The two dynamical parametrizations reproduce the low magnitude of INP concentrations and also shows improvement in simulating the cloud and radiative properties during this case study. Among all tested INP schemes, the SSA-driven M18 performs best in simulating the magnitude of LWP and surface radiation. Although it slightly overcorrects the SW biases, it is physically consistent with its slight underestimation of observed INP concentrations. Improvements to the SSA flux parameterizations to increase emissions, as suggested by Regayre et al. (2020), may mitigate this underestimation.

The microphysical and radiative responses to altered INP concentrations are strongly regime-dependent. During the deep, frontal MIX periods, reducing INP concentrations effectively suppresses glaciation, significantly enhances LWP, and largely mitigates the surface SW radiation biases. The M18 scheme shows the most pronounced improvement in cloud reflectivity during these frontal passages. Conversely, during the shallow, post-frontal SLW periods, cloud and radiation properties show negligible sensitivity to changes in INP concentrations due to a lack of pre-existing ice. Radiosonde comparisons and extreme sensitivity tests reveal that this insensitivity is driven by a lack of boundary layer moisture as a first order, while cloud microphysics is of second order importance. The models systematically fail to reproduce the sharp temperature inversion capping the boundary layer, leading to excessive entrainment of dry air. Furthermore, an underestimation of cyclone intensity in the large-scale forcing limits moisture transport. Consequently, these shallow clouds are macrophysically starved of water vapor, rendering microphysical INP adjustments ineffective.

While the online implementation of dynamical marine INP schemes marks a significant step forward, several uncertainties remain. Current aerosol schemes exhibit limitations in accurately predicting marine aerosol emissions under extreme wind conditions and cold sea surface temperatures. Additionally, relying solely on satellite-derived chlorophyll-a as a proxy for organic aerosol emissions misses the complex biogeochemical processes in the SO. Furthermore, the empirical M18 and W15 formulas themselves carry uncertainties when applied to extreme cold temperatures or when accounting for the physiochemical

© Author(s) 2026. CC BY 4.0 License.

selectivity of aerosol emissions. More importantly, the absence of a dust parametrization limits the model's ability to fully close the INP budget at cold cloud tops.

For future work, improving the representation of mixed-phase clouds over the SO and Antarctic requires a synergistic approach. First, future model development should prioritize refining boundary layer turbulence and entrainment parametrizations to correctly simulate capping inversions and maintain moisture in post-frontal regimes. Second, improving the fidelity of large-scale meteorological forcing and initial conditions is essential to ensure realistic synoptic representation and moisture advection. Moreover, future high-resolution models should transition towards fully coupled atmosphere-ocean biogeochemical frameworks. This will allow dynamic INP schemes to be driven by real-time marine biological fluxes and realistic dust transport, providing a physically robust representation of aerosol-cloud interactions across all cloud regimes over the SO. Ultimately, the insights and constraints derived from these high-resolution modelling studies must be integrated to improve the parameterizations of global Earth System Models, ensuring a physically robust representation of these cloud regimes on a climate scale to mitigate the uncertainties in climate projections (Schneider et al., 2017; Zelinka et al., 2020; McFarquhar et al., 2021).

Appendix A: Additional figures

Code and data availability. Cloud and aerosol observations from the CAPRICORN-2 campaign are publicly available on the CSIRO Data Access Portal (https://data.csiro.au/collection/csiro:46392v3). INP measurements can be retrieved from the SOCRATES EOL repository (https://data.eol.ucar.edu/dataset/552.133). UM simulations along the ship track, along with the data visualization code are available on Zenodo repository (https://doi.org/10.5281/zenodo.20637823). ERA5 reanalysis fields are provided by the C3S Climate Data Store (https://cds.climate.copernicus.eu). MODIS Aqua chlorophyll-a concentrations and NSIDC sea ice data are accessible via the NASA OceanColor Web (https://oceancolor.gsfc.nasa.gov) and the NSIDC portal (https://nsidc.org/data), respectively. The EMC^2 software is open-source and accessible via GitHub (https://github.com/ARM-DOE/EMC2).

Author contributions. ZP completed the model simulations, analysis and writing of this work. SLF, MDM, MTW, SPA, and AP contributed to the project planning of this paper. SLF and MTW provided guidance on the model set-up. All authors contributed to the revisions of this paper.

Competing interests. The contact author has declared that none of the authors has any competing interests.

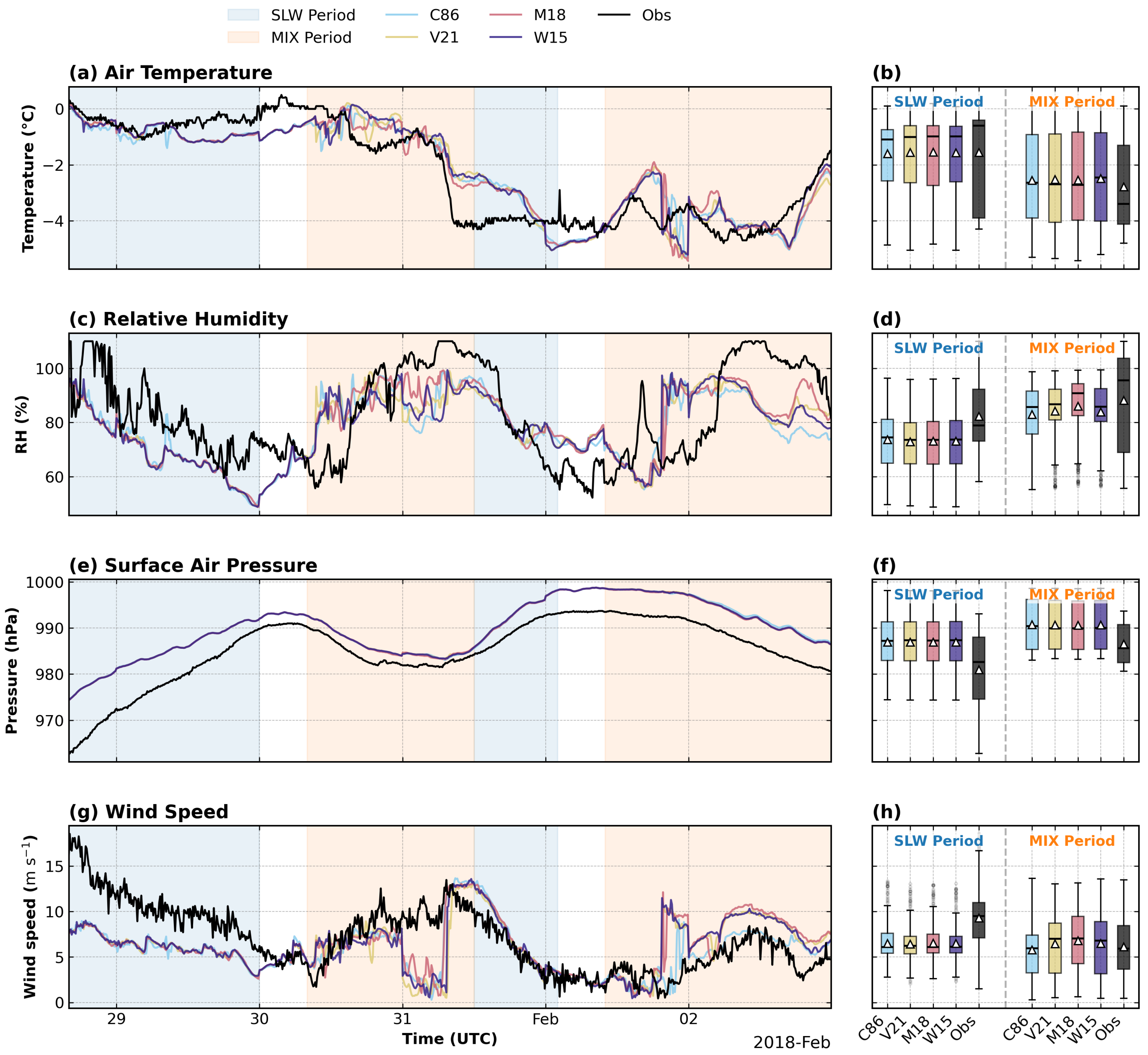

Figure A1. Timeseries comparisons between the shipborne observations (black lines) and the UM configurations (colored lines) for **(a)** surface air temperature (°C), **(c)** relative humidity (%), **(e)** surface air pressure (hPa), and **(g)** 10-meter wind speed ($\mathrm{m\,s^{-1}}$). The light blue and light orange background shadings denote the SLW and MIX periods, respectively. The corresponding right-hand panels **(b, d, f, h)** present statistical boxplots of these variables grouped by the defined cloud regimes. The boxplot conventions are identical to those described in Figure 6.

© Author(s) 2026. CC BY 4.0 License.

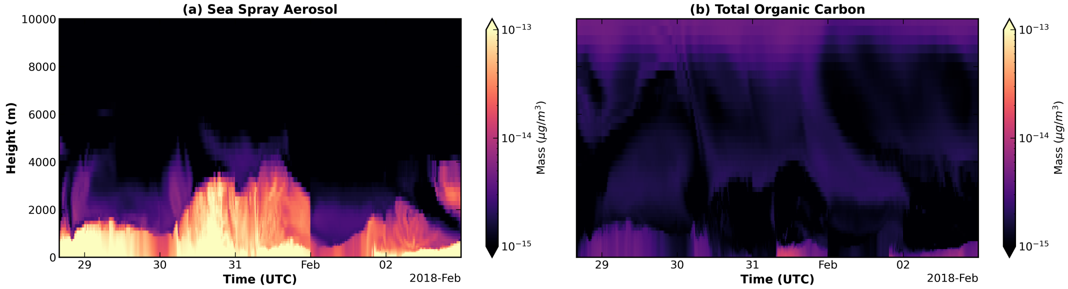

Figure A2. Time-height cross-sections of the simulated prognostic aerosol mass concentrations along the ship track during the case study period. **(a)** Sea Spray Aerosol (SSA) mass concentration ($\mu\mathrm{g\,m^{-3}}$), representing the sum of the soluble accumulation and coarse modes derived from the GLOMAP-mode scheme. **(b)** Total Organic Carbon (TOC) mass concentration ($\mu\mathrm{g\,m^{-3}}$), utilized as the proxy for marine organic aerosols.

Acknowledgements. This project received grant funding from the Australian Government as part of the Antarctic Science Collaboration Initiative program, under the Australian Antarctic Program Partnership, ASCI000002. This research was undertaken with the assistance of resources and services from the National Computational Infrastructure (projects jk72, xp65, and rt52), which is supported by the Australian Government. Zhangcheng Pei acknowledges the PhD scholarship provided by China Scholarship Council (CSC) Grant (202206330006) from the Ministry of Education of the People's Republic of China. Zhangcheng Pei was supported by the Atmospheric Radiation Measurement (ARM) user facility, a U.S. Department of Energy (DOE) Office of Science user facility managed by the Biological and Environmental Research Program through an Atmospheric Systems Research grant (grant no. DE-SC0022001). Zhangcheng Pei and Sonya L. Fiddes acknowledges the Australian Earth System Simulator National Research Infrastructure, funded by the Australian Government's National Collaborative Research Infrastructure Strategy, for their maintenance of virtual environments, code and model support. This research was supported by a grant of sea time on RV Investigator (2441) from the CSIRO Marine National Facility (https://ror.org/01mae9353). The authors would like to acknowledge the teams at the NASA Earthdata, NSIDC, and ECMWF for making the data used in this work available.

https://doi.org/10.5194/egusphere-2026-3541
Preprint. Discussion started: 9 July 2026
© Author(s) 2026. CC BY 4.0 License.

References

Alexander, S. and Protat, A.: Cloud properties observed from the surface and by satellite at the northern edge of the Southern Ocean, Journal of Geophysical Research: Atmospheres, 123, 443–456, 2018.

Alexander, S., McFarquhar, G., Marchand, R., Protat, A., Vignon, É., Mace, G., and Klekociuk, A.: Mixed-phase clouds and precipitation in Southern Ocean cyclones and cloud systems observed poleward of 64° S by ship-based cloud radar and lidar, Journal of Geophysical Research: Atmospheres, 126, e2020JD033 626, 2021.

Atlas, R. L., Bretherton, C. S., Blossey, P. N., Gettelman, A., Bardeen, C., Lin, P., and Ming, Y.: How Well Do Large-Eddy Simulations and Global Climate Models Represent Observed Boundary Layer Structures and Low Clouds Over the Summertime Southern Ocean?, Journal of Advances in Modeling Earth Systems, 12, e2020MS002 205, https://doi.org/10.1029/2020MS002205, 2020.

Best, M. J., Pryor, M., Clark, D., Rooney, G. G., Essery, R. L., Menard, C. B., Edwards, J., Hendry, M., Porson, A., Gedney, N., et al.: The Joint UK Land Environment Simulator (JULES), model description–Part 1: energy and water fluxes, Geoscientific Model Development, 4, 677–699, 2011.

Bhatti, Y. A., Revell, L. E., Schuddeboom, A. J., McDonald, A. J., Archibald, A. T., Williams, J., Venugopal, A. U., Hardacre, C., and Behrens, E.: The sensitivity of Southern Ocean atmospheric dimethyl sulfide (DMS) to modeled oceanic DMS concentrations and emissions, Atmospheric Chemistry and Physics, 23, 15 181–15 196, 2023.

Bodas-Salcedo, A., Williams, K. D., Ringer, M. A., Beau, I., Colin, J., Dufresne, J.-L., Koshiro, T., Stevens, B., Wang, Z., and Yokohata, T.: Origins of the solar radiation biases over the Southern Ocean in CFMIP2 models, Journal of Climate, 27, 41–56, https://doi.org/10.1175/JCLI-D-13-00169.1, 2014.

Bodas-Salcedo, A., Hill, P., Furtado, K., Williams, K., Field, P., Manners, J., Hyder, P., and Kato, S.: Large contribution of supercooled liquid clouds to the solar radiation budget of the Southern Ocean, Journal of Climate, 29, 4213–4228, 2016.

Boutle, I., Eyre, J., and Lock, A.: Seamless stratocumulus simulation across the turbulent gray zone, Monthly Weather Review, 142, 1655–1668, 2014.

Burrows, S. M., Hoose, C., Pöschl, U., and Lawrence, M. G.: Ice nuclei in marine air: biogenic particles or dust?, Atmospheric Chemistry and Physics, 13, 245–267, https://doi.org/10.5194/acp-13-245-2013, 2013.

Bush, M., Allen, T., Bain, C., Boutle, I., Edwards, J., Finnenkoetter, A., Franklin, C., Hanley, K., Lean, H., Lock, A., et al.: The first Met Office unified model–JULES regional atmosphere and land configuration, RAL1, Geoscientific Model Development, 13, 1999–2029, 2020.

Bush, M., Boutle, I., Edwards, J., Finnenkoetter, A., Franklin, C., Hanley, K., Jayakumar, A., Lewis, H., Lock, A., Mittermaier, M., et al.: The second Met Office Unified Model–JULES Regional Atmosphere and Land configuration, RAL2, Geoscientific Model Development, 16, 1713–1734, 2023.

Bush, M., Flack, D. L., Lewis, H. W., Bohnenstengel, S. I., Short, C. J., Franklin, C., Lock, A. P., Best, M., Field, P., McCabe, A., et al.: The third Met Office Unified Model-JULES Regional Atmosphere and Land Configuration, RAL3, Geoscientific Model Development, 2024, 3819–3855, 2025.

Clark, D., Mercado, L., Sitch, S., Jones, C., Gedney, N., Best, M., Pryor, M., Rooney, G., Essery, R., Blyth, E., et al.: The Joint UK Land Environment Simulator (JULES), model description–Part 2: carbon fluxes and vegetation dynamics, Geoscientific Model Development, 4, 701–722, 2011.

Cooper, W. A.: Ice initiation in natural clouds, Meteorological Monographs, 21, 29–32, 1986.

© Author(s) 2026. CC BY 4.0 License.

Daily, M. I., Robinson, J., Finney, D. L., Raif, E. N., McQuaid, J. B., Sanchez-Marroquin, A., Hu, K., Lloyd, G., Flynn, M., Field, P. R., et al.: Ice-nucleating particle and cloud ice crystal concentrations associated with developing summertime deep convective clouds in south-western USA, Journal of Geophysical Research: Atmospheres, 131, e2024JD043 236, 2026.

Delanoë, J., Protat, A., Vinson, J.-P., Brett, W., Caudoux, C., Bertrand, F., Du Châtelet, J. P., Hallali, R., Barthes, L., Haeffelin, M., et al.: BASTA: A 95-GHz FMCW Doppler radar for cloud and fog studies, Journal of Atmospheric and Oceanic Technology, 33, 1023–1038, 2016.

DeMott, P. J., Prenni, A. J., Liu, X., Kreidenweis, S. M., Petters, M. D., Twohy, C. H., Richardson, M., Eidhammer, T., and Rogers, D.: Predicting global atmospheric ice nuclei distributions and their impacts on climate, Proceedings of the National Academy of Sciences, 107, 11 217–11 222, 2010.

DeMott, P. J., Hill, T. C., McCluskey, K. S., Prather, K. A., Collins, D. B., Sullivan, R. C., Ruppel, M. J., Mason, R. H., Irish, V. E., Lee, T., et al.: Sea spray aerosol as a unique source of ice nucleating particles, Proceedings of the National Academy of Sciences, 113, 5797–5803, https://doi.org/10.1073/pnas.1514034112, 2016.

Doddridge, E. W., Hobbs, W. R., Auger, M., Boyd, P. W., Chua, S. M., Cook, S., Corney, S., Emmerson, L., Fraser, A. D., Heil, P., et al.: Impacts of Antarctic summer sea-ice extremes, PNAS nexus, 4, pgaf164, 2025.

Edwards, J. and Slingo, A.: Studies with a flexible new radiation code. I: Choosing a configuration for a large-scale model, Quarterly Journal of the Royal Meteorological Society, 122, 689–719, 1996.

Eyring, V., Bony, S., Meehl, G. A., Senior, C. A., Stevens, B., Stouffer, R. J., and Taylor, K. E.: Overview of the Coupled Model Intercomparison Project Phase 6 (CMIP6) experimental design and organization, Geoscientific Model Development, 9, 1937–1958, 2016.

Fiddes, S. L., Protat, A., Mallet, M. D., Alexander, S. P., and Woodhouse, M. T.: Southern Ocean cloud and shortwave radiation biases in a nudged climate model simulation: does the model ever get it right?, Atmospheric Chemistry and Physics, 22, 14 603–14 630, 2022.

Fiddes, S. L., Woodhouse, M. T., Mallet, M. D., Lamprey, L. J., Humphries, R. S., Protat, A., Alexander, S. P., Hayashida, H., Putland, S., Miljevic, B., et al.: The ACCESS-AM2 climate model underestimates aerosol concentration in the Southern Ocean; improving aerosol representation could be problematic for the global energy balance, Atmospheric Chemistry and Physics, 25, 16 451–16 477, 2025.

Field, P. R., Hill, A., Shipway, B., Furtado, K., Wilkinson, J., Miltenberger, A., Gordon, H., Grosvenor, D. P., Stevens, R., and Van Weverberg, K.: Implementation of a double moment cloud microphysics scheme in the UK Met Office regional numerical weather prediction model, Quarterly Journal of the Royal Meteorological Society, 2023.

Furtado, K. and Field, P.: The role of ice microphysics parametrizations in determining the prevalence of supercooled liquid water in high-resolution simulations of a Southern Ocean midlatitude cyclone, Journal of the Atmospheric Sciences, 74, 2001–2021, 2017.

Furtado, K., Field, P., Boutle, I., Morcrette, C., and Wilkinson, J.: A physically based subgrid parameterization for the production and maintenance of mixed-phase clouds in a general circulation model, Journal of the Atmospheric Sciences, 73, 279–291, 2016.

Gantt, B., Meskhidze, N., Facchini, M., Rinaldi, M., Ceburnis, D., and O'Dowd, C.: Wind speed dependent size-resolved parameterization for the organic mass fraction of sea spray aerosol, Atmospheric Chemistry and Physics, 11, 8777–8790, 2011.

Gantt, B., Johnson, M., Meskhidze, N., Sciare, J., Ovadnevaite, J., Ceburnis, D., and O'Dowd, C.: Model evaluation of marine primary organic aerosol emission schemes, Atmospheric Chemistry and Physics, 12, 8553–8566, 2012.

Garnesson, P., Mangin, A., Fanton d'Andon, O., Demaria, J., and Bretagnon, M.: The CMEMS GlobColour chlorophyll a product based on satellite observation: multi-sensor merging and flagging strategies, Ocean Science, 15, 819–830, 2019.

Gettelman, A., Hannay, C., Bacmeister, J. T., Neale, R. B., Pendergrass, A. G., Danabasoglu, G., Lamarque, J.-F., Fasullo, J. T., Bailey, D. A., Lawrence, D. M., et al.: High climate sensitivity in the Community Earth System Model version 2 (CESM2), Geophysical Research Letters, 46, 8329–8337, https://doi.org/10.1029/2019GL083978, 2019.

Gettelman, A., Bardeen, C., McCluskey, C. S., Järvinen, E., Stith, J., Bretherton, C., McFarquhar, G., Twohy, C., D'Alessandro, J., and Wu, W.: Simulating observations of Southern Ocean clouds and implications for climate, Journal of Geophysical Research: Atmospheres, 125, e2020JD032 619, 2020.

Gong, S.: A parameterization of sea-salt aerosol source function for sub-and super-micron particles, Global biogeochemical cycles, 17, 2003.

Gordon, H., Field, P. R., Abel, S. J., Barrett, P., Bower, K., Crawford, I., Cui, Z., Grosvenor, D. P., Hill, A. A., Taylor, J., et al.: Development of aerosol activation in the double-moment Unified Model and evaluation with CLARIFY measurements, Atmospheric Chemistry and Physics, 20, 10 997–11 024, 2020.

Guyot, A., Protat, A., Alexander, S. P., Klekociuk, A. R., Kuma, P., and McDonald, A.: Detection of supercooled liquid water containing clouds with ceilometers: development and evaluation of deterministic and data-driven retrievals, Atmospheric Measurement Techniques, 15, 3663–3681, 2022.

Haëntjens, N., Boss, E., and Talley, L. D.: Revisiting O cean C olor algorithms for chlorophyll a and particulate organic carbon in the S outhern O cean using biogeochemical floats, Journal of Geophysical Research: Oceans, 122, 6583–6593, 2017.

Hallett, J. and Mossop, S.: Production of secondary ice particles during the riming process, Nature, 249, 26–28, 1974.

Hawker, R. E., Miltenberger, A. K., Wilkinson, J. M., Hill, A. A., Shipway, B. J., Cui, Z., Cotton, R. J., Carslaw, K. S., Field, P. R., and Murray, B. J.: The temperature dependence of ice-nucleating particle concentrations affects the radiative properties of tropical convective cloud systems, Atmospheric Chemistry and Physics, 21, 5439–5461, 2021.

Herbert, R. J., Sanchez-Marroquin, A., Grosvenor, D. P., Pringle, K. J., Arnold, S. R., Murray, B. J., and Carslaw, K. S.: Gaps in our understanding of ice-nucleating particle sources exposed by global simulation of the UK Earth System Model, Atmospheric Chemistry and Physics, 25, 291–325, 2025.

Hines, K. M., Bromwich, D. H., Silber, I., Russell, L. M., and Bai, L.: Predicting Frigid Mixed-Phase Clouds for Pristine Coastal Antarctica, Journal of Geophysical Research: Atmospheres, 126, e2021JD035 112, 2021.

Hoose, C. and Möhler, O.: Heterogeneous ice nucleation on atmospheric aerosols: a review of results from laboratory experiments, Atmospheric Chemistry and Physics, 12, 9817–9854, https://doi.org/10.5194/acp-12-9817-2012, 2012.

Huang, B., Liu, C., Banzon, V., Freeman, E., Graham, G., Hankins, B., Smith, T., and Zhang, H.-M.: Improvements of the daily optimum interpolation sea surface temperature (DOISST) version 2.1, Journal of Climate, 34, 2923–2939, 2021.

Huang, Y., Siems, S. T., Manton, M. J., and Thompson, G.: An evaluation of WRF simulations of clouds over the Southern Ocean with A-Train observations, Monthly Weather Review, 142, 647–667, 2014.

Hulswar, S., Simó, R., Galí, M., Bell, T. G., Lana, A., Inamdar, S., Halloran, P. R., Manville, G., and Mahajan, A. S.: Third revision of the global surface seawater dimethyl sulfide climatology (DMS-Rev3), Earth System Science Data, 14, 2963–2987, 2022.

Hyder, P., Edwards, J. M., Allan, R. P., Hewitt, H. T., Bracegirdle, T. J., Gregory, J. M., Wood, R. A., Meijers, A. J., Mulcahy, J., Field, P., et al.: Critical Southern Ocean climate model biases traced to atmospheric model cloud errors, Nature communications, 9, 3625, 2018.

Jaeglé, L., Quinn, P., Bates, T., Alexander, B., and Lin, J.-T.: Global distribution of sea salt aerosols: new constraints from in situ and remote sensing observations, Atmospheric Chemistry and Physics, 11, 3137–3157, 2011.

Kanji, Z. A., Ladino, L. A., Wex, H., Boies, A., Chou, C., Hoose, C., Lündsted, T., Mohr, C., and Sierau, B.: Overview of ice nucleating particles, Meteorological Monographs, 58, 1–1, https://doi.org/10.1175/AMSMONOGRAPHS-D-16-0006.1, 2017.

Kay, J. E., Wall, C., Yettella, V., Medeiros, B., Hannay, C., Caldwell, P., and Bitz, C.: Global climate impacts of fixing the Southern Ocean shortwave radiation bias in the Community Earth System Model (CESM), Journal of Climate, 29, 4617–4636, 2016.

Knight, C. L., Mallet, M. D., Alexander, S. P., Fraser, A. D., Protat, A., and McFarquhar, G. M.: Cloud properties and boundary layer stability above Southern Ocean sea ice and coastal Antarctica, Journal of Geophysical Research: Atmospheres, 129, e2022JD038 280, 2024.

Kulmala, M., Laaksonen, A., and Pirjola, L.: Parameterizations for sulfuric acid/water nucleation rates, Journal of Geophysical Research: Atmospheres, 103, 8301–8307, 1998.

Lana, A., Bell, T., Simó, R., Vallina, S. M., Ballabrera-Poy, J., Kettle, A., Dachs, J., Bopp, L., Saltzman, E., Stefels, J., et al.: An updated climatology of surface dimethlysulfide concentrations and emission fluxes in the global ocean, Global biogeochemical cycles, 25, 2011.

Liss, P. S. and Merlivat, L.: Air-sea gas exchange rates: Introduction and synthesis, in: The role of air-sea exchange in geochemical cycling, pp. 113–127, Springer, 1986.

Mace, G. G., Protat, A., Humphries, R. S., Alexander, S. P., McFarquhar, G. M., Ding, J., and Mace, S.: Mixed-phase clouds over the Southern Ocean as observed from satellite and surface based lidar and radar, Journal of Geophysical Research: Atmospheres, 126, e2021JD034 600, https://doi.org/10.1029/2021JD034600, 2021.

Mallet, M. D., Humphries, R. S., Fiddes, S. L., Alexander, S. P., Altieri, K., Angot, H., Anilkumar, N., Bartels-Rausch, T., Creamean, J., Dall'Osto, M., et al.: Untangling the influence of Antarctic and Southern Ocean life on clouds, Elementa: Science of the Anthropocene, 11, 2023.

Mallet, M. D., Miljevic, B., Humphries, R. S., Mace, G. G., Alexander, S. P., Protat, A., Chambers, S., Cravigan, L., DeMott, P. J., Fiddes, S., et al.: Biological enhancement of cloud droplet concentrations observed off East Antarctica, npj Climate and Atmospheric Science, 8, 113, 2025.

Mann, G. W., Carslaw, K., Spracklen, D., Ridley, D., Manktelow, P., Chipperfield, M., Pickering, S., and Johnson, C.: Description and evaluation of GLOMAP-mode: A modal global aerosol microphysics model for the UKCA composition-climate model, Geoscientific Model Development, 3, 519–551, 2010.

Mann, G. W., Carslaw, K., Ridley, D., Spracklen, D., Pringle, K., Merikanto, J., Korhonen, H., Schwarz, J., Lee, L., Manktelow, P., et al.: Intercomparison of modal and sectional aerosol microphysics representations within the same 3-D global chemical transport model, Atmospheric Chemistry and Physics, 12, 4449–4476, 2012.

McCluskey, C. S., Hill, T. C., Humphries, R. S., Rauker, A. M., Moreau, S., Strutton, P., Chambers, S. D., Williams, A. G., McRobert, I., Ward, J., et al.: Observations of ice nucleating particles over Southern Ocean waters, Geophysical Research Letters, 45, 11–989, 2018a.

McCluskey, C. S., DeMott, P. J., Ma, P.-L., and Burrows, S. M.: Numerical representations of marine ice-nucleating particles in remote marine environments evaluated against observations, Geophysical Research Letters, 46, 7838–7847, 2019.

McCluskey, C. S., Gettelman, A., Bardeen, C. G., DeMott, P. J., Moore, K. A., Kreidenweis, S. M., Hill, T. C., Barry, K. R., Twohy, C. H., Toohey, D. W., et al.: Simulating Southern Ocean aerosol and ice nucleating particles in the Community Earth System Model version 2, Journal of Geophysical Research: Atmospheres, 128, e2022JD036 955, 2023.

McCluskey, K. S., Ovadnevaite, J., Rinaldi, M., Atkinson, J., Belosi, F., Ceburnis, D., Marullo, S., Hill, T. C., and DeMott, P. J.: Marine and terrestrial organic ice-nucleating particles in pristine marine to continentally influenced background air, Journal of Geophysical Research: Atmospheres, 123, 6196–6212, https://doi.org/10.1029/2017JD028033, 2018b.

McCoy, D. T., Burrows, S. M., Wood, R., Grosvenor, D. P., Elliott, S. M., Ma, P.-L., and Rasch, P. J.: Natural aerosols explain seasonal and spatial patterns of Southern Ocean cloud albedo, Science Advances, 1, e1500 157, https://doi.org/10.1126/sciadv.1500157, 2015.

McDonald, A., Kuma, P., Panell, M., Petterson, O., Plank, G., Rozliaiani, M., and Whitehead, L.: Evaluating cloud properties at Scott Base: Comparing ceilometer observations with ERA5, JRA55, and MERRA2 reanalyses using an instrument simulator, Journal of Geophysical Research: Atmospheres, 130, e2024JD041 754, 2025.

McFarquhar, G. M., Bretherton, C. S., Marchand, R., Protat, A., DeMott, P. J., Alexander, S. P., Roberts, G. C., Twohy, C. H., Toohey, D., Siems, S., et al.: Observations of clouds, aerosols, precipitation, and surface radiation over the Southern Ocean: An overview of CAPRICORN, MARCUS, MICRE, and SOCRATES, Bulletin of the American Meteorological Society, 102, E894–E928, 2021.

Meier, W. N., Fetterer, F., Windnagel, A. K., Stewart, J. S., and Stafford, T.: NOAA/NSIDC Climate Data Record of Passive Microwave Sea Ice Concentration, https://doi.org/10.7265/b18j-z797, g02202. Date accessed: 25 May 2026, 2026.

Meyers, M. P., DeMott, P. J., and Cotton, W. R.: New primary ice-nucleation parameterizations in an explicit cloud model, Journal of Applied Meteorology and Climatology, 31, 708–721, https://doi.org/10.1175/1520-0450(1992)031<0708:NPINPI>2.0.CO;2, 1992.

Moore, K. A., Hill, T. C., McCluskey, C. S., Twohy, C. H., Rainwater, B., Toohey, D. W., Sanchez, K. J., Kreidenweis, S. M., and DeMott, P. J.: Characterizing ice nucleating particles over the Southern Ocean using simultaneous aircraft and ship observations, Journal of Geophysical Research: Atmospheres, 129, e2023JD039 543, 2024.

Mulcahy, J. P., Johnson, C., Jones, C. G., Povey, A. C., Scott, C. E., Sellar, A., Turnock, S. T., Woodhouse, M. T., Abraham, N. L., Andrews, M. B., et al.: Description and evaluation of aerosol in UKESM1 and HadGEM3-GC3. 1 CMIP6 historical simulations, Geoscientific Model Development, 13, 6383–6423, 2020.

Murray, B. J., O'Sullivan, D., Atkinson, J. D., Webb, M. E., , et al.: Ice nucleation by particles immersed in supercooled cloud droplets, Chemical Society Reviews, 41, 6519–6554, https://doi.org/10.1039/C2CS35200A, 2012.

NASA Ocean Biology Processing Group: Aqua MODIS Level-3 Global Mapped Chlorophyll (CHL) Data, version 2022.0, https://doi.org/10.5067/AQUA/MODIS/L3M/CHL/2022.0, date accessed: 25 May 2026, 2025.

Noh, Y.-J., Miller, S. D., Heidinger, A. K., Mace, G. G., Protat, A., and Alexander, S. P.: Satellite-based detection of daytime supercooled liquid-topped mixed-phase clouds over the Southern Ocean using the Advanced Himawari Imager, Journal of Geophysical Research: Atmospheres, 124, 2677–2701, 2019.

Pei, Z., Fiddes, S. L., French, W. J. R., Alexander, S. P., Mallet, M. D., Kuma, P., and McDonald, A.: Assessing the cloud radiative bias at Macquarie Island in the ACCESS-AM2 model, Atmospheric Chemistry and Physics, 23, 14 691–14 714, 2023.

Pei, Z., Fiddes, S. L., Mallet, M., Alexander, S. P., Furtado, K., Knight, C. L., Roff, G. L., Smith, D. K. E., Protat, A., McDonald, A. J., et al.: Refining the Simulation of Mixed-phase Clouds Over Coastal Antarctica with a Tailored Ice Nucleating Particle Parameterization, Authorea Preprints, 2025a.

Pei, Z., Fiddes, S. L., Mallet, M. D., Alexander, S. P., Furtado, K., Roff, G., Protat, A., McDonald, A., and French, W. J. R.: Simulating mixed-phase clouds over coastal Antarctica during a significant snowfall event in a high-resolution regional model, Journal of Geophysical Research: Atmospheres, 130, e2024JD042 311, 2025b.

Prather, K. A., Bertram, T. H., Grassian, V. H., Deane, G. B., Stokes, M. D., DeMott, P. J., Aluwihare, L. I., Palenik, B. P., Azam, F., Seinfeld, J. H., et al.: Bringing the ocean into the laboratory to probe the chemical complexity of sea spray aerosol, Proceedings of the National Academy of Sciences, 110, 7550–7555, 2013.

Price, R., Orr, A., Field, P., Mace, G., and Protat, A.: Simulation of Cloud Processes Over Offshore Coastal Antarctica Using the High-Resolution Regional UK Met Office Unified Model With Interactive Aerosols, Journal of Geophysical Research: Atmospheres, 130, e2024JD042 109, 2025.

© Author(s) 2026. CC BY 4.0 License.

Protat, A., Delanoë, J., Bouniol, D., Heymsfield, A., Bansemer, A., and Brown, P.: Evaluation of ice water content retrievals from cloud radar reflectivity and temperature using a large airborne in situ microphysical database, Journal of applied meteorology and climatology, 46, 557–572, 2007.

Protat, A., CSIRO, and Marine National Facility: RV Investigator BOM Atmospheric Data Overview (2016 onwards). v3, https://doi.org/10.25919/5f688fcc97166, data Collection, 2020.

Quinn, P. K., Collins, D. B., Grassian, V. H., Prather, K. A., and Bates, T. S.: Chemistry and related properties of freshly emitted sea spray aerosol, Chemical reviews, 115, 4383–4399, 2015.

Regayre, L. A., Schmale, J., Johnson, J. S., Tatzelt, C., Baccarini, A., Henning, S., Yoshioka, M., Stratmann, F., Gysel-Beer, M., Grosvenor, D. P., et al.: The value of remote marine aerosol measurements for constraining radiative forcing uncertainty, Atmospheric Chemistry and Physics, 20, 10 063–10 072, 2020.

Revell, L. E., Kremser, S., Hartery, S., Harvey, M., Mulcahy, J. P., Williams, J., Morgenstern, O., McDonald, A. J., Varma, V., Bird, L., et al.: The sensitivity of Southern Ocean aerosols and cloud microphysics to sea spray and sulfate aerosol production in the HadGEM3-GA7. 1 chemistry–climate model, Atmospheric Chemistry and Physics, 19, 15 447–15 466, 2019.

Russell, L. M., Moore, R. H., Burrows, S. M., and Quinn, P. K.: Ocean flux of salt, sulfate, and organic components to atmospheric aerosol, Earth-Science Reviews, 239, 104 364, 2023.

Salter, M. E., Zieger, P., Acosta Navarro, J. C., Grythe, H., Kirkevåg, A., Rosati, B., Riipinen, I., and Nilsson, E. D.: An empirically derived inorganic sea spray source function incorporating sea surface temperature, Atmospheric Chemistry and Physics, 15, 11 047–11 066, 2015.

Schneider, T., Lan, S., Stuart, A., and Teixeira, J.: Earth system modeling 2.0: A blueprint for models that learn from observations and targeted high-resolution simulations, Geophysical Research Letters, 44, 12–396, 2017.

Silber, I., Jackson, R. C., Fridlind, A. M., Ackerman, A. S., Collis, S., Verlinde, J., and Ding, J.: The Earth Model Column Collaboratory (EMC 2) v1. 1: an open-source ground-based lidar and radar instrument simulator and subcolumn generator for large-scale models, Geoscientific Model Development, 15, 901–927, 2022.

Smith, D. K., Renfrew, I. A., van den Heuvel, F., Lachlan-Cope, T., Crawford, I., Bower, K., Flynn, M., Evans, M. D., Abel, S. J., and Field, P.: The impact of mixed-phase cloud processes on simulating Southern Ocean clouds and their radiative effect, Journal of Geophysical Research: Atmospheres, 130, e2025JD044 452, 2025.

Sotiropoulou, G., Vignon, É., Young, G., Morrison, H., O'Shea, S. J., Lachlan-Cope, T., Berne, A., and Nenes, A.: Secondary ice production in summer clouds over the Antarctic coast: an underappreciated process in atmospheric models, Atmospheric Chemistry and Physics, 21, 755–771, https://doi.org/10.5194/acp-21-755-2021, 2021.

Storelvmo, T. and Tan, I.: The Wegener-Bergeron-Findeisen process–Its discovery and vital importance for weather and climate, Meteorologische Zeitschrift, 24, 455–461, 2015.

Trenberth, K. E. and Fasullo, J. T.: Simulation of present-day and twenty-first-century energy budgets of the Southern Oceans, Journal of Climate, 23, 440–454, https://doi.org/10.1175/2009JCLI3152.1, 2010.

Twohy, C. H., DeMott, P. J., Russell, L. M., Toohey, D. W., Rainwater, B., Geiss, R., Sanchez, K. J., Lewis, S., Roberts, G. C., Humphries, R. S., et al.: Cloud-nucleating particles over the Southern Ocean in a changing climate, Earth's Future, 9, e2020EF001 673, 2021.

Van Weverberg, K., Morcrette, C. J., Boutle, I., Furtado, K., and Field, P. R.: A bimodal diagnostic cloud fraction parameterization. Part I: Motivating analysis and scheme description, Monthly Weather Review, 149, 841–857, 2021.

Vergara-Temprado, J., Murray, B. J., Wilson, T. W., O'Sullivan, D., Pringle, K. J., Ardon-Dryer, K., Bertram, A. K., Burrows, S. M., Ceburnis, D., DeMott, P. J., et al.: Contribution of feldspar and marine organic aerosols to global ice nucleating particle concentrations, Atmospheric Chemistry and Physics, 17, 3637–3658, 2017.

Vergara-Temprado, J., Miltenberger, A. K., Furtado, K., Grosvenor, D. P., Shipway, B. J., Hill, A. A., Wilkinson, J. M., Field, P. R., Murray, B. J., and Carslaw, K. S.: Strong control of Southern Ocean cloud reflectivity by ice-nucleating particles, Proceedings of the National Academy of Sciences, 115, 2687–2692, 2018.

Vignon, É., Alexander, S., DeMott, P., Sotiropoulou, G., Gerber, F., Hill, T., Marchand, R., Nenes, A., and Berne, A.: Challenging and improving the simulation of mid-level mixed-phase clouds over the high-latitude Southern Ocean, Journal of Geophysical Research: Atmospheres, 126, e2020JD033 490, 2021.

Willett, M., Brooks, M., Bushell, A., Earnshaw, P., Smith, S., Tomassini, L., Best, M., Boutle, I., Brooke, J., Edwards, J. M., et al.: The Met Office Unified Model Global Atmosphere 8.0 and JULES Global Land 9.0 configurations, Geoscientific Model Development, 19, 1473–1517, 2026.

Wilson, T. W., Ladino, L. A., Alpert, P. A., Breckels, M. N., Brooks, I. M., Browse, J., Burrows, S. M., Carslaw, K. S., Huffman, J. A., Judd, C., et al.: A marine biogenic source of atmospheric ice-nucleating particles, Nature, 525, 234–238, https://doi.org/10.1038/nature14986, 2015.

Wood, N., Staniforth, A., White, A., Allen, T., Diamantakis, M., Gross, M., Melvin, T., Smith, C., Vosper, S., Zerroukat, M., et al.: An inherently mass-conserving semi-implicit semi-Lagrangian discretization of the deep-atmosphere global non-hydrostatic equations, Quarterly Journal of the Royal Meteorological Society, 140, 1505–1520, 2014.

Woodward, S.: Modeling the atmospheric life cycle and radiative impact of mineral dust in the Hadley Centre climate model, Journal of Geophysical Research: Atmospheres, 106, 18 155–18 166, 2001.

Zelinka, M. D., Myers, T. A., McCoy, D. T., Po-Chedley, S., Caldwell, P. M., Ceppi, P., Klein, S. A., and Taylor, K. E.: Causes of higher climate sensitivity in CMIP6 models, Geophysical Research Letters, 47, e2019GL085 782, 2020.

Zhao, X., Liu, X., Burrows, S. M., and Shi, Y.: Effects of marine organic aerosols as sources of immersion-mode ice-nucleating particles on high-latitude mixed-phase clouds and atmospheric radiation, Atmospheric Chemistry and Physics, 21, 2305–2327, https://doi.org/10.5194/acp-21-2305-2021, 2021.

Zhao, X., Lin, Y., Yin, Y., Lu, C., Wang, Y., Wang, M., Krueger, S. K., DeMott, P. J., and Mace, G. G.: Important Ice Processes Are Missed by the Community Earth System Model in Southern Ocean Mixed-Phase Clouds, Journal of Geophysical Research: Atmospheres, 128, e2022JD037 513, https://doi.org/10.1029/2022JD037513, 2023.